Engineering Structures 302 (2024) 117364

Contents lists available at ScienceDirect

Engineering Structures

journal homepage: www.elsevier.com/locate/engstruct

Fibre orientation in SFRC slabs and consequences for punching shear and flexural resistance

Diego Hernández Fraile [a,*,1], Enrico Faccin [b], Fausto Minelli [b], Giovanni Plizzari [b], Aurelio Muttoni [a]

[a] *School of Architecture, Civil and Environmental Engineering, École Polytechnique Fédérale de Lausanne EPFL, Switzerland*
[b] *University of Brescia UNIBS, Department of Civil, Environmental, Architectural Engineering and Mathematics, Italy*

ARTICLE INFO

Keywords:
Steel Fibre Reinforced Concrete (SFRC)
Flat slabs
Punching shear
Flexural resistance
Micro-computed tomography
Fibre spatial variability
Fibre orientation

ABSTRACT

The use of steel fibre reinforced concrete (SFRC) is a well-known method for enhancing the punching and flexural resistances of flat slabs. The structural performance of SFRC elements depends significantly on the fibre distribution and orientation, which are typically unknown. One of the largest uncertainties regarding the performance and reliability of SFRC concerns the determination of its post-cracking mechanical properties in the real structural element, normally performed via standardised tests. However, due to differences in element sizes and casting procedures, and to the presence of rebars, the fibre spatial distribution and orientation in the standard specimens differ in general from those of the structural member. Several researchers have studied the correlation between the orientation of fibres and the mechanical performance of SFRC, yet tests were rarely carried out under representative conditions of the actual behaviour of the target structural member. The present paper analyses the spatial distribution and orientation of steel fibres in six SFRC flat slabs that were previously tested in concentric punching at the University of Brescia. The aim of this work is to analyse the fibre orientation and spatial distribution in structural elements. Cores were extracted from the specimens after the punching tests and scanned using micro-computed tomography (μ-CT) to reconstruct the fibre skeleton. The fibre arrangement was analysed focusing on the variation of the fibre spatial distribution and orientation through the slab thickness. A formulation to express the actual fibre dispersion in concrete is proposed, and effectiveness factors are defined to reflect the efficacy of fibres in punching shear and flexure, based on their location in the slab thickness. Pseudo-horizontal fibre orientations are found to be governing, with closer distributions to a 2D scenario for thicker slabs and higher fibre contents. Furthermore, the influence of flexural reinforcement on the fibre orientation has been observed to be significant. The observed fibre orientations are detrimental for the direct transfer of shear forces across cracks, but are favourable for enhancing the flexural capacity of the slab.

1. Introduction

Punching failures of reinforced concrete (RC) flat slabs without shear reinforcement are governed by the capacity of concrete to transfer shear forces through inclined cracks forming around the column [5,6]. The addition of steel fibres is an effective method for enhancing this shear-transfer capacity and, consequently, the punching resistance of the connection [7–12]. Steel fibres also increase the flexural resistance of the cross section, with a direct effect on the slab's overall flexural behaviour. This flexural enhancement indirectly improves the slab's punching resistance [13]. Extensive research on steel fibre reinforced concrete (SFRC) has been carried out to evaluate the crack-bridging capacity of steel fibres, the mechanical interaction between fibres and matrix, and the response at the material level [14–22]. At the structural level, the use of SFRC with moderate fibre dosages (below 2% in volume) has resulted in a cost-effective method for improving the ultimate punching resistance of slab-column connections [9–11]. The crack-bridging capacity of the steel fibres also enhances the deformation capacity of the slab [7,8], which is important in punching due to the brittleness of failure in slabs without shear reinforcement [6,11].

The most important mechanical property of SFRC is the crack-bridging capacity of the fibres, generally represented by the post-cracking residual tensile stress (σ_{tf}) vs. crack opening (w) relationship

---

* Correspondence to: EPFL ENAC IIC IBETON, GC B2 475 (Bâtiment GC), Station 18, CH-1015 Lausanne, Switzerland.
E-mail address: diego.hernandezfraile@epfl.ch (D. Hernández Fraile).

[1] ORCID: https://orcid.org/0000-0003-1235-1564

https://doi.org/10.1016/j.engstruct.2023.117364
Received 30 August 2023; Received in revised form 22 November 2023; Accepted 13 December 2023

Nomenclature

Symbols, variables, and parameters

A_j, A_M	horizontal projected area of the surface of the critical shear crack: in layer j, in the mean layer
B	slab side length
$b_{0,j}$	punching-shear control perimeter of layer j [1,2]
c	column side length
d_{top}, d_{bot}	average effective depth of the slab for hogging and sagging moments
d_f	steel fibre diameter
f_c	uniaxial concrete compressive strength
f_{R1}, $f_{R,3}$	tensile residual stresses corresponding to SLS and ULS CMOD
h, h_{core}	slab thickness, concrete core height
l_f, $l_{f,dev}$, Δl	straight or projected fibre length, developed fibre length, fibre length interval
k_{eff}, k_V, k_{Mhog}, k_{Msag}	layer effectiveness factor: general expression, in shear, in hogging and in sagging
n_j	number of horizontal layers for the division of the critical shear crack
$N_{f,meas}$	measured total number of fibres in a concrete core
r_{core}	distance between slab centre and axis of concrete core
s_{top}, s_{bot}	rebar spacing of top and bottom reinforcement layers
V, $V_{R,f}$	punching shear force, steel fibre contribution to the punching resistance of a slab
V_{core}	net volume of concrete core
$V_{f,meas,tot}$	total measured volume of fibres in a concrete core
w	crack opening
x, x'	reference axis for the measurement of fibre orientations within the horizontal plane, arbitrary axis for the computation of the directions of maximum and minimum fibre alignment
z, z_j, Δz	height with respect to slab bottom face, height of slab layer j, slab layer thickness
α	generic direction for the evaluation of the fibre orientation factor
β, $\Delta\beta$	angle formed by the axis of a steel fibre and the horizontal plane, interval of angle β
φ, $\Delta\varphi$	angle formed by the horizontal fibre projection and scanning axis x, interval of angle φ
φ_0, $\varphi_{0,min}$, $\varphi_{0,max}$	angle between axis x and arbitrary axis x', angle between axis x and the horizontal direction of minimum, maximum fibre alignment
$Ø_{top}$, $Ø_{bot}$, $Ø_{core}$	nominal rebar diameter in the top and bottom reinforcement layers, nominal diameter of concrete core.
σ_{tf}	residual tensile stress across a crack in steel-fibre reinforced concrete
$\eta_{or,\alpha}$, $\eta_{or,hmin}$, $\eta_{or,hmax}$, $\eta_{or,z}$	fibre orientation factor: in generic direction α, along the horizontal direction with minimum fibre alignment, maximum fibre alignment, and vertical direction
η_{sv}	fibre spatial variation factor
η_{eff}, η_V, η_{Mhog}, η_{Msag}	fibre global effectiveness factor: general expression, in shear, in hogging, and in sagging
ρ_f, $\rho_{f,\alpha}$, $\rho_{f,meas}$, $\rho_{f,\alpha,meas}$	nominal fibre volume ratio, nominal effective fibre volume ratio in generic direction α, measured fibre volume ratio, effective fibre volume ratio in generic direction α
$\Delta\rho_{f,meas}$	measured fibre volume ratio in an interval of fibre lengths, vertical or horizontal orientations
θ	angle between fibre axis and generic direction α
ψ	slab rotation

Acronyms and abbreviations

CSCT, CSC	Critical Shear Crack Theory, Critical Shear Crack
μ-CT	Micro-Computed Tomography
RC, SFRC	Reinforced Concrete, Steel Fibre Reinforced Concrete
SLS, ULS	Serviceability Limit State, Ultimate Limit State
VEM	Variable Engagement Model [3,4]
CMOD	Crack Mouth Opening Displacement

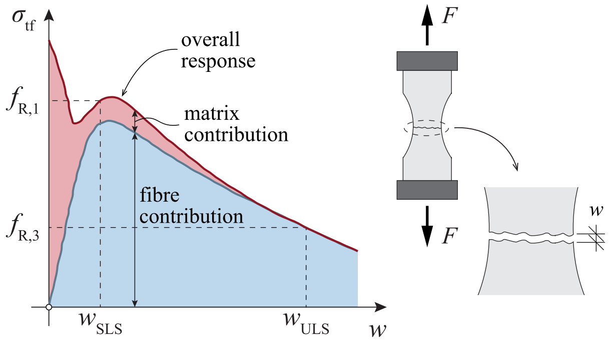

Fig. 1. Tensile post-cracking constitutive law of SFRC (adapted from [13]).

(Fig. 1). It can be directly obtained through uniaxial tensile tests or from bending tests, using either a method known as “Inverse Analysis” or simplified procedures provided by structural codes [19]. Several research efforts have been devoted to the development of models that can predict the residual tensile strength of SFRC, useful both for research and structural design. Some models are based on empirical formulations for computing the Serviceability Limit State (SLS, $f_{R,1} = \sigma_{tf}(w_{SLS})$) and Ultimate Limit State (ULS, $f_{R,3} = \sigma_{tf}(w_{ULS})$) post-cracking tensile parameters of SFRC [23–25]. They are mainly based on large databases of standard bending tests on small prismatic beams. The Variable Engagement Model (VEM, [3,4]), on the other hand, presents an analytical formulation based on mechanical principles that assumes an isotropic distribution of fibres in concrete. For punching shear, some empirical models have been proposed to directly estimate the resistance of a SFRC slab-column connection [8,10,12]. Other research works have combined a model for determining the residual tensile strength of SFRC with the formulation of the Critical Shear Crack Theory (CSCT, [6]) for punching failures; they have shown that this strategy provides accurate strength predictions [11,13,23].

The distribution and orientation of steel fibres in the concrete matrix are two fundamental parameters for the mechanical response of SFRC. Different techniques have been used for their study: direct fibre counting at a crack [26,27], electrical resistivity [28,29], or Alternating Current-Impedance Spectroscopy [29], among others. Micro-Computed Tomography, or CT-scanning, has become a widespread, non-invasive technique to study the fibre orientation in concrete [27,28,30,31–38]. It allows reconstructing the fibre skeleton in three dimensions from 2D slices and extracting very detailed information of each individual fibre, yet it is normally limited to small-sized specimens [38]. Furthermore, some works have studied the theoretical orientation of fibres in concrete from an analytical perspective [26,39–42].

Many researchers have analysed the orientation of fibres in concrete to link it with the material’s post-cracking properties [27,30,32–37,43,44,45]. Some works have also studied the influence of fresh concrete flow on the fibre orientation, using different concrete mixes, pouring schemes and specimen dimensions [30,32–34,43,44–46]. The use of concretes with higher flowability, such as self-compacting concrete (SCC), has led to fibres oriented in horizontal planes and perpendicular to the concrete flow for plate-like specimens [33,34,43,44–46], and parallel to the flow for beam-like specimens [36,46]. The concrete pouring location has also been found to influence the fibre distribution, notably farther away from the pouring position [34]. Vibrating the concrete has been reported to favour the horizontal arrangement of fibres [40]. The presence of steel rebars has also been observed to have an influence on the fibre orientation, acting as a constraint to the flow [47]. In some studies, cores have been extracted from existing structural elements to perform fibre orientation analyses [36]. Of particular interest is the work of Aidarov et al. [48], where a full-scale SFRC, 2-by-2 bay flat slab was tested under a uniformly distributed load; fibre density and orientation were measured from cores extracted post-mortem from different slab regions. In practice, the use of SFRC for building flat slabs is gradually becoming more common [49–51]: while some projects have used steel fibres as a complement to conventional flexural rebars, others have deployed steel fibres as the sole slab reinforcement.

The reference fibre orientation for the comparison of measurements in SFRC specimens depends mainly on the structural application and on the specimen geometry and dimensions. For instance, structural codes consider different approaches: while Model Code 2010 [1] considers as a reference an isotropic fibre orientation, the new generation of Eurocode 2, in its Annex L [2], takes as a reference the orientation in beam tests according to EN14651 [52]. In this research, the measured orientation of fibres is compared to an isotropic three-dimensional fibre orientation, due to the relevance of vertically-oriented fibres to effectively transfer shear forces across inclined cracks [13].

This paper analyses the fibre spatial distribution and orientation in six SFRC slabs with conventional reinforcement, with different sizes and fibre volume ratios (also referred in the literature as volume fraction). The main aim of the work is to establish a direct correlation between the fibre dispersion in flat slabs and the enhancement of their punching shear resistance thanks to the fibre addition. These analyses were performed on a complete series of slabs where specimen size and fibre content were varied. Thus, they allowed understanding how these two parameters influence the fibre orientation, and the fibres' contribution to the slab punching resistance. The slabs were previously tested in concentric punching at the University of Brescia (UNIBS) [53] (an independent paper describing these results is currently in preparation), and cylindrical cores were extracted outside the punching-damaged slab region to study the fibre orientation in the crack planes. By estimating the fibre orientation in a slab specimen that has already been tested, a direct correlation can be established between this parameter and the enhancement of the punching resistance.

The extracted cores were scanned using micro-computed tomography and the fibre skeleton was reconstructed in three dimensions using software Avizo [54]. The reconstruction results are analysed to understand how fibres are spatially distributed and oriented within the thickness of the slabs. Spatial variation and fibre orientation factors are defined to establish a relationship between a scenario with an isotropic, homogeneous distribution, and the measured fibre spatial distribution and orientation. Moreover, effectiveness factors are proposed to reflect the relative influence of fibres at different heights within the slab thickness on the overall fibre contribution to punching and flexure. The two groups of factors are then combined and applied to the tested slabs to better understand the actual SFRC properties for the evaluation of a slab's punching and flexural resistances.

Most research efforts in the literature that perform both fibre orientation analyses and statical testing have done so on characterisation beams rather than on actual structural members (e.g. [27,30,32–37,43,44,45]). When fibre orientation analyses have been made on actual structural members, they have seldom been tested prior to the fibre analysis [36]. This work, in a similar fashion as done in [48] for the flexural response of a flat slab, combines both approaches to provide a baseline for the assessment of the contribution of steel fibres to the punching and flexural resistances of flat slabs.

2. Specimens, casting procedure and measurements

2.1. Preceding research: punching tests on SFRC flat slabs

An experimental campaign on nine RC flat slabs was carried out at the University of Brescia (UNIBS) [53]. This campaign analysed two main parameters, namely the fibre dosage and the size of the specimens. Three slab sizes, with thicknesses of 250 (S250), 125 (S125) and 68 (S68) mm were tested. All geometric parameters except the aggregate size, nominal concrete cover and fibre type, were scaled down proportionally; they are presented in Table 1. Specimens were square of side B, resting on a central square column of side c. The top flexural reinforcement (hogging reinforcement in flat slabs) was placed in two orthogonal layers, parallel to the specimen sides. Its ratio was kept constant at approximately 0.8% for all slab sizes by adapting the rebar diameter and spacing. Slabs S125 and S250 incorporated bottom reinforcement as well, with a ratio of approximately 0.25%. For each slab size, three specimens were produced: a reference specimen without fibres, and two slabs with 40 and 80 kg/m^3 of steel fibre dosages (equivalent to 0.5% and 1.0% by volume, respectively). The fibres used were end-hooked with a length of 35 mm and a diameter of 0.6 mm. Table 1 and Fig. 2a present the main properties of the six fibre-reinforced slabs. Fig. 2b,c show the flexural reinforcement arrangement of the slabs in plan view and cross section, respectively. They also illustrate the reinforcement parameters included in Table 1. The reference slabs without fibres are not considered in this work. The nomenclature of the slabs includes an "S" followed by the slab thickness (in mm) and the fibre volume ratio (volume %), separated by a hyphen. For further information on the slabs, the reader is referred to [53].

Slabs with the same fibre content were cast from the same batch of concrete. The concrete compressive strength f_c was estimated for each slab from uniaxial compression tests on six cubes (150 ×150 ×150 mm) tested at an age of 28 days, plus four cylinders ($Ø_{cyl} \times h_{cyl} =$ 100 ×200 mm) tested at 50 days; their average values are reported in Table 1. The post-cracking tensile behaviour of the SFRC was characterised according to EN 14651 [52]. For each fibre content (0.5 or 1.0%), eight notched beams of standard dimensions were tested. The mean values of the residual tensile strength parameters $f_{R,1}$ (for a crack mouth opening displacement CMOD of 0.5 mm) and $f_{R,3}$ (for a CMOD of 2.5 mm) are also reported in Table 1. For further details on the characterisation procedure and the dispersion of the results (e.g., the coefficient of variation) of the SFRC properties, the reader is referred to [53].

Table 2 describes the concrete mixes used for the SFRC slabs. The maximum aggregate size was 20 mm, the water-to-cement ratio was 0.55, and superplasticizer Mapei Dynamon Xtend W400 N was added to the mix, with a dosage of 4 and 4.8 kg/m^3 for the mixes with 0.5% and 1.0% fibre volume ratios, respectively. The consistency of the fresh concrete was evaluated through slump tests, with similar measured slumps of about 200 mm for the two concrete mixes.

Different casting procedures were used due to the variable size of the specimens. In particular, slabs S68 and S125 were cast using a bucket located at the centre of the specimen (Fig. 2d), while slabs S250 were cast placing the bucket at four locations around the slab centre, as schematically shown in Fig. 2e. All slabs were cast in a single pour. Concrete was vibrated after each bucket pour for approximately 3–4 min, using hand vibrators (vibrators of 36 mm in diameter were used for slabs S68, while vibrators of both 36 and 50 mm in diameter were used for slabs S125 and S250).

2.2. Core drilling and micro-computed tomography scans

After testing the slabs in concentric punching [53], three cores from each specimen were extracted for the fibre spatial distribution and

Table 1
Summary of slab properties.

Slab ID	B [mm]	h [mm]	c [mm]	d_{top} [mm]	$Ø_{\mathrm{top}}$ [mm]	s_{top} [mm]	d_{bot} [mm]	$Ø_{\mathrm{bot}}$ [mm]	s_{bot} [mm]	f_c [MPa]	ρ_f [%]	$f_{R,1}$ [MPa]	$f_{R,3}$ [MPa]
S68-0,5	870	68	65	53	6	70	-	-	-	25	0.5	3.18	2.72
S68-1,0				55						28	1.0	5.93	4.94
S125-0,5	1620	125	130	100	10	90	108	8	180	25	0.5	3.18	2.72
S125-1,0				105						28	1.0	5.93	4.94
S250-0,5	3240	250	260	203	18	150	218	10	135	25	0.5	3.18	2.72
S250-1,0				198						28	1.0	5.93	4.94

orientation analyses. The cores' location was selected on the basis of two criteria: (i) to avoid regions affected by the punching failure (i.e., the region presenting shear cracks, delamination cracks or visible flexural cracks); and (ii) to extract the cores as close as possible to the failure shear cracks to be as representative as possible of the fibre arrangement in the punching-sensitive region. The location and identification of each core are indicated in Fig. 2f. The cores were cylindrical with a nominal diameter ($Ø_{\mathrm{core}}$) of 75 mm, as shown in Fig. 2g; the measured values are reported in Table 3. The digitally reconstructed depth of each core, defined as h_{core} in Fig. 2g, corresponds to the height of the core that was analysed, measured from the bottom slab face. Rebars from the top and bottom reinforcement layers were sometimes extracted with the core. For instance, Fig. 4 presents the results of a core which contained flexural rebars, while Fig. 5 shows the results of a core that did not contain them. The distance between the centre of the slab and the centre of each core (r_{core}) is indicated in Fig. 2f. The values are reported in Table 3, see Section 3.2.

All 18 cores were scanned using the micro-computed tomography technique (μ-CT). The scans were performed at the Interdisciplinary Platform for X-ray micro-tomography (PIXE) of École Polytechnique Fédérale de Lausanne, Switzerland (EPFL), using their RX-SOLUTIONS Ultratom 160/230 kV micro-CT system. The tomography data was collected at an acceleration voltage of 200 kV and 270μA beam current, captured using a 2176 × 1792 px plane sensor. The voxel size was 56 μm.

The 2D high-resolution slices obtained from the μ-CT scans were reconstructed in three dimensions using software Avizo [54]. After all the slice data for one core were imported in the software, a first filtering was performed to remove the measuring noise. Fibres in Avizo [54] are typically delimited by two end nodes. Two different techniques were used for fibre detection and reconstruction:

1. Initially, fibres were automatically detected using the skeletonization functionality. However, the crossing of fibres in space triggered the detection of fake nodes in some fibres at the crossing location, and even short fibres joining both fake nodes. This issue has already been reported in the literature [31], and it was solved by using the filament editor. It allowed removing manually nodes and fibres, as well as joining fibre segments. This technique had a limitation since, due to the similar reflection properties of fibres and rebars, they could not be clearly separated at the level of the top flexural rebars. For this reason, the reconstruction could only be made until right below the top bars.
2. To improve the reconstruction results, a different method was used for several cores. It required to manually segment the different materials: matrix, voids, rebars and fibres. After isolating the fibres, extension FiberX was used to detect them automatically, searching for tube-like entities. This solved the problem of the skeletonization technique and allowed analysing the full height of the cores.

3. Fibre spatial distribution and orientation results

The visualisation of the 3D-reconstructed cores provided useful information on the fibre arrangement in the slabs. The extracted results included (see Fig. 3 for their geometrical definition):

1. The developed fibre length $l_{\mathrm{f,dev}}$, which accounts for the length of the fibre's straight segment plus the end hooks, developed along the straight segment axis.
2. The straight or projected fibre length l_{f}, defined as the straight distance between the two fibre end points or as the length of the fibre's projection along its axis.
3. The fibre orientation with respect to the horizontal plane, defined by angle β, complementary to the angle between the fibre axis and the core vertical axis z.
4. The orientation of the horizontal fibre projection in the XY plane, defined by angle φ between the horizontal projection axis and scan axis x (variable for different cores, but always contained in the horizontal plane).
5. The coordinates of the two end nodes of each fibre.

This data was used to quantify the spatial variability of the fibre density, identifying the regions with higher concentrations of fibres. The actual orientation of fibres in space was also measured; it was later compared to an isotropic distribution (equal probability of a fibre to be oriented in any direction of space). The cores were analysed considering the full concrete volume and by horizontal layers, dividing the cores in slices which were defined taking into account the location of the flexural reinforcement and the bottom formwork (to evaluate wall effects).

3.1. 3D reconstruction results

Fig. 4 shows the reconstruction of core S68–0,5-E, extracted from the slab with a thickness of 68 mm and 0.5% of fibre dosage (S68–0,5). From the 3D view of the core (Fig. 4b), one can observe the different components at the outer core surfaces: the dark blue represents the cementitious matrix, the aggregates are in lighter shades of blue, and the steel rebars and fibres are in yellow. Fibre fragments, most probably cut in the extraction process, can be observed at the core lateral surface. Fig. 4a illustrates the slab cross-section with the reinforcement bars. Fig. 4c, d show the views of the top and bottom core regions, respectively. These views comprise the first millimetres of the core near the slab top and bottom surfaces. They clearly show the wall effect due to both the bottom formwork and the flattening of the top concrete surface after casting [28,35]. Interestingly, in this core the number of horizontal fibres is higher at the top than at the bottom core end, suggesting a stronger wall effect.

The steel fibres (in dark red colour) and reinforcing steel (in light blue) have been isolated in Fig. 4e. Even though they had very similar reflective properties, they could be effectively separated manually for their independent analysis. Fig. 4f shows the view of the fibres from a similar perspective than Fig. 4b,e with a colour gradient to show the orientation of the fibres with respect to the horizontal plane (angle β). Horizontal fibres are shown in red colour and vertical fibres in blue. As can be observed, fibres tended to be oriented horizontally, most notably between the flexural reinforcement and the top slab surface. Interestingly, the region with the largest number of vertical or pseudo-vertical fibres was directly below the reinforcement bars. This can be explained by fibres falling through the spaces between the two orthogonal rebar layers at the end of the concrete pour, hence having no space to flow in the horizontal direction. Fewer fibres can be observed near the

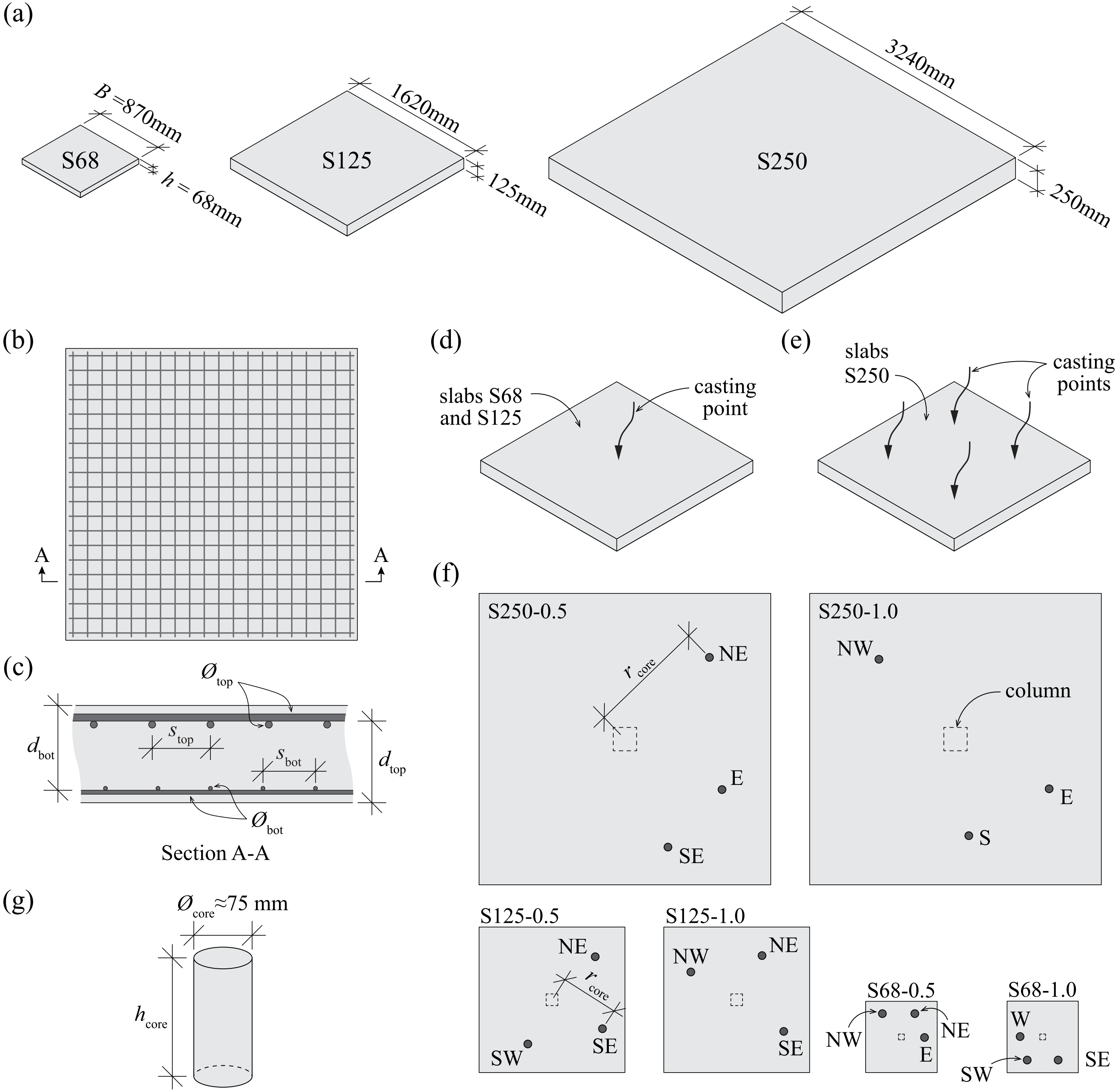

Fig. 2. Information of slabs: (a) main slab dimensions; flexural reinforcement arrangement (b) in plan view and (c) along cross-section A-A; (d) casting point for slabs S125 and S68; (e) casting points for slabs S250; (f) location and identification of the scanned cores in each slab; and (g) core geometry.

Table 2
Concrete mixes.

Component(dosages in [kg/m^3])	Fibre volume ratio (ρ_f)	
	0.5%	1.0%
Sand (aggregate size < 2 mm)	795	795
Gravel (aggregate size 2 - 20 mm)	1034	1034
Cement 32.5 N (CEM II-B-LL)	320	320
Water	175	175
Superplasticizer	4	4.8

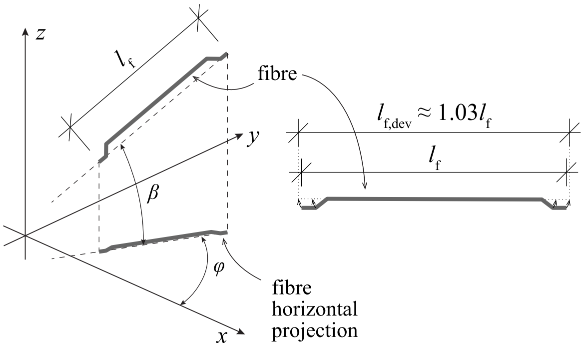

Fig. 3. Definition of the geometrical fibre parameters used in this work.

bottom formwork.

Fig. 5 shows the same results for core S250–0,5-E. In this case, no reinforcing bars were cut in the core extraction, neither in the top nor in the bottom layers. Nevertheless, the influence of the rebars near the core location can be observed in the fibre distribution and orientation (Fig. 5d). For this reason, the location of the top and bottom rebar layers are indicated in Fig. 5a. Similar wall effects as in core S68–0,5-E, both at the top and bottom core regions (Fig. 5c), can be observed, again with a larger number of pseudo-flat fibres at the top slab face. In this case, this could additionally be due to the interference of the bottom layers of reinforcement in the fibre flow. The bottom rebars were placed with a clear cover of 22 mm and they could have impeded non-horizontal fibres to flow under them, thus limiting the presence of fibres between the bottom rebar layers and the formwork.

Fibres were mainly horizontal in this core, with large concentrations of quasi-horizontal fibres on top of the bottom reinforcement and in the region between the top reinforcement and the slab surface. Vertical fibres can be observed sparsely distributed along the slab thickness, with higher concentrations in two particular regions: around the top and bottom reinforcement layers, and right below the top rebars. A region of reduced fibre content can also be observed under the top reinforcement layers, further confirming the interference of the flexural rebars on the concrete flow [47].

3.2. *Main scanning results and fibre spatial variation and orientation factors*

The measured fibre volume ratio in each concrete core $\rho_{f,meas}$ can be computed with Eq. (1):

$$\rho_{f,meas} = \frac{V_{f,meas,tot}}{V_{core}} \tag{1}$$

where $V_{f,meas,tot}$ is the total fibre volume measured in the core of net concrete volume V_{core} (without the volume of the reinforcement bars). In a scenario of a non-isotropic fibre orientation, the effective fibre volume ratio in a generic direction α, $\rho_{f,\alpha,meas}$, can be calculated from the fibre orientation measurements with Eq. (2):

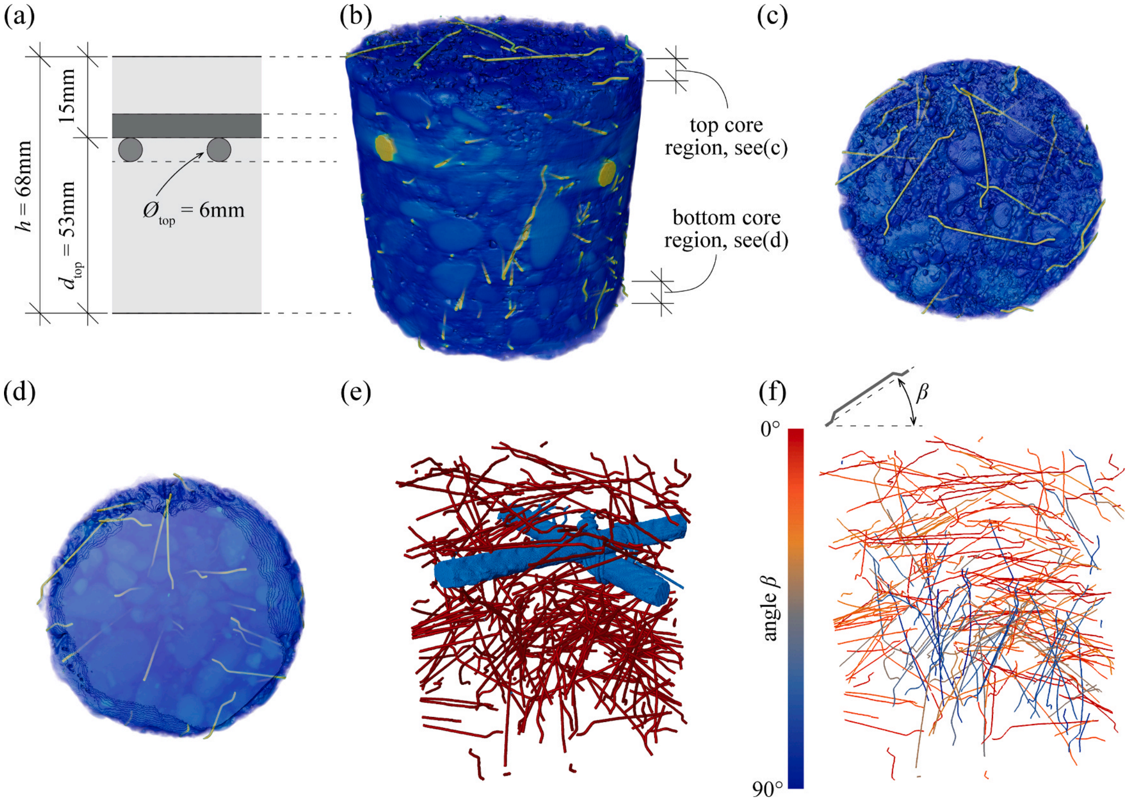

Fig. 4. Reconstruction results of core S68–0,5-E: (a) slab cross-section; (b) 3D core representation; (c) end view of the top core region; (d) end view of the bottom core region; (e) 3D view of the reconstructed fibres (red) and the flexural rebars (blue); and (f) steel fibre skeleton with a colour gradient to illustrate the angle β between the fibre axis and the horizontal plane (the reader is referred to the online paper version for the colour codes).

Table 3
Full scan results and fibre spatial variation and orientation factors.

Core	r_{core} [mm]	h_{core} [mm]	$Ø_{core}$ [mm]	ρ_f [%]	$\rho_{f,meas}$ [%]	η_{sv}	$\eta_{or,hmax}$	$\eta_{or,hmin}$	$\eta_{or,z}$
S68-0,5-E	270	73	75.7	0.5	0.58	1.16	1.22	0.93	0.82
S68-0,5-NE(*)	310	39	74.6	0.5	0.46	0.92	1.18	0.87	0.92
S68-0,5-NW	340	73	75.2	0.5	0.42	0.85	1.08	0.97	0.92
					Average (μ)	0.97	1.16	0.93	0.89
					St. Dev (σ)	0.16	0.07	0.05	0.06
S68-1,0-W(*)	260	45	74.1	1.0	0.86	0.86	1.21	0.99	0.77
S68-1,0-SW(*)	320	46	75.4	1.0	0.65	0.65	1.14	1.01	0.83
S68-1,0-SE(*)	320	45	76.2	1.0	0.97	0.97	1.22	0.92	0.80
					Average (μ)	0.83	1.19	0.98	0.80
					St. Dev (σ)	0.16	0.05	0.05	0.03
S125-0,5-NE(*)	680	87	74.8	0.5	0.43	0.85	1.28	0.83	0.84
S125-0,5-SW(*)	650	79	74.5	0.5	0.40	0.80	1.00	0.90	1.10
S125-0,5-SE(*)	560	101	74.8	0.5	0.38	0.77	1.06	0.90	1.03
					Average (μ)	0.81	1.11	0.88	0.99
					St. Dev (σ)	0.04	0.15	0.04	0.13
S125-1,0-NW(*)	600	87	74.6	1.0	0.77	0.77	1.31	0.87	0.79
S125-1,0-NE(*)	570	78	74.9	1.0	0.80	0.80	1.19	1.04	0.72
S125-1,0-SE(*)	630	92	75.1	1.0	0.65	0.65	1.23	1.02	0.75
					Average (μ)	0.74	1.24	0.98	0.75
					St. Dev (σ)	0.08	0.06	0.09	0.03
S250-0,5-SE(*)	1290	219	74.8	0.5	0.39	0.78	1.36	0.99	0.57
S250-0,5-E	1220	259	75.5	0.5	0.44	0.87	1.28	1.00	0.63
S250-0,5-NE	1310	254	75.7	0.5	0.44	0.88	1.32	1.00	0.60
					Average (μ)	0.85	1.32	1.00	0.60
					St. Dev (σ)	0.05	0.04	0.01	0.03
S250-1,0-E	1180	259	75.7	1.0	0.84	0.84	1.24	1.12	0.55
S250-1,0-S(*)	1080	219	75.3	1.0	0.88	0.88	1.26	1.06	0.59
S250-1,0-NW	1230	256	76.6	1.0	1.07	1.07	1.25	0.92	0.78
					Average (μ)	0.93	1.25	1.03	0.64
					St. Dev (σ)	0.12	0.01	0.10	0.12

(*)indicates cores for which the skeletonization reconstruction technique was used, hence the full core height could not be analysed (the reader is referred to Section 2.2 for a detailed explanation on the reason for this). This is reflected in the core height column h_{core}

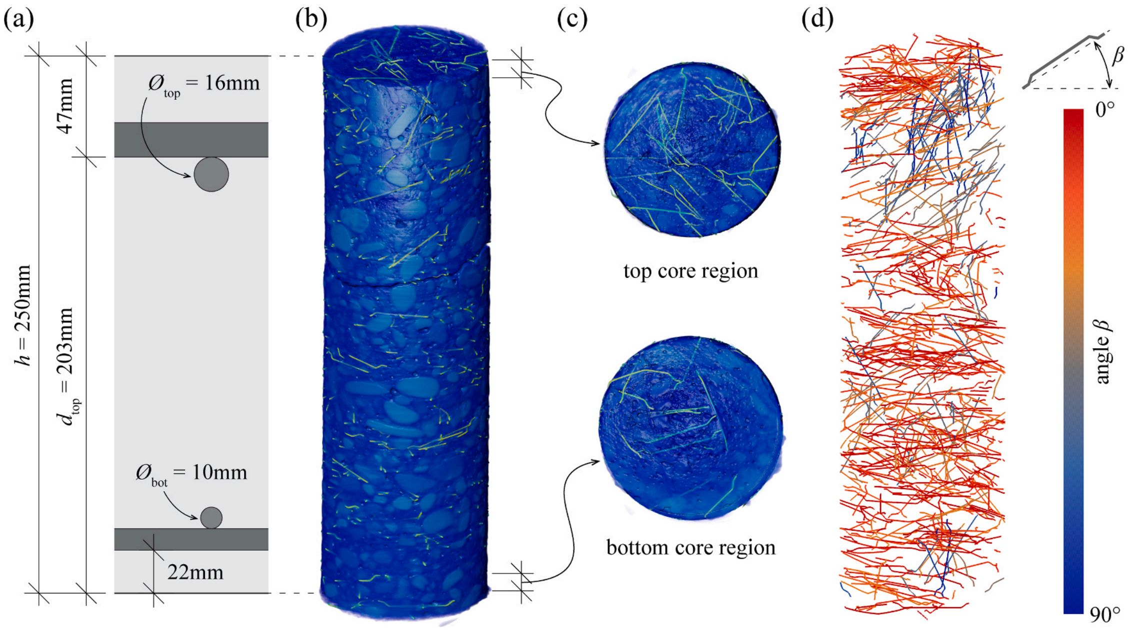

Fig. 5. Reconstruction results of core S250–0,5-E: (a) slab cross-section; (b) 3D core representation; (c) end views of the top and bottom core regions; and (d) steel fibre skeleton with a colour gradient to illustrate the angle β between the fibre axis and the horizontal plane (the reader is referred to the online paper version for the colour codes).

$$\rho_{f,\alpha,meas} = \frac{d_f^{\,2}}{h_{core}\cdot Ø_{core}^{\,2}}\cdot \sum_{i=1}^{N_{f,meas}} \left(l_{f,dev,i}\cdot \cos\theta_i\right) \tag{2}$$

where θ_i is the angle between the fibre axis and generic direction α. It has to be mentioned that, for the sake of simplicity, the net concrete volume V_{core} has been replaced in Eq. (2) by the gross volume, since the difference between both values is small (less than 3%). For the ideal case of an isotropic fibre orientation, Aveston and Kelly [14] established that the effective fibre volume ratio $\rho_{f,\alpha}$ in all directions is $\rho_f/2$. This means that, for the general case of non-uniform fibre spatial distribution and anisotropic fibre orientation, the actual measured fibre volume ratio in a generic direction α can be expressed with Eq. (3):

$$\rho_{f,\alpha,meas} = \frac{1}{2} \cdot \rho_f \cdot \eta_{sv} \cdot \eta_{or,\alpha} \tag{3}$$

where factor $\eta_{\mathrm{sv}} = \rho_{\mathrm{f,meas}}/\rho_{\mathrm{f}}$ describes the spatial variation of fibres within the concrete element (related to factor κ_{G} defined in Annex L of the new generation of Eurocode 2 [2] as a function of the member size), and the fibre orientation factor $\eta_{\mathrm{or},\alpha}$ represents the difference between the actual fibre orientation and an isotropic scenario (its concept is similar to factor κ_{O} defined in Annex L of new Eurocode 2 [2]). Its formulation is presented in Appendix A. For the ideal case of uniformly distributed fibres and an isotropic fibre orientation, spatial variation factor η_{sv} and fibre orientation factor $\eta_{\mathrm{or},\alpha}$ in all directions would be equal to 1.0.

The scanning results of the analysed cores are presented in Table 3. The first three columns indicate the distance from the centre of the slab to the axis of the core r_{core}, the reconstructed core height h_{core}, and the measured core diameter $\varnothing_{\mathrm{core}}$. The two last measures were obtained from the μ-CT data. The cores where the skeletonization reconstruction technique was used had h_{core} values smaller than the slab thickness, as their full height could not be analysed, see Section 2.2. Moreover, for the cores where the full height was reconstructed, measured core heights deviated slightly from the nominal slab thickness. These deviations were always smaller than 1 cm for the 250 mm thick slabs and 5 mm for the 68 mm thick slabs.

The last four columns of Table 3 present the results of the spatial variation and fibre orientation factors for all cores. The measured spatial variation factor values (η_{sv}) indicate that the steel fibres were not homogeneously distributed in the slab. Regarding the orientation factors, three directions were considered: the vertical direction ($\eta_{\mathrm{or,z}}$) to reflect the direct contribution of fibres to the punching shear resistance of the slabs; the maximum horizontal direction ($\eta_{\mathrm{or,hmax}}$), which represents the direction in the horizontal plane in which the effective fibre volume ratio is maximum in the core; and the minimum horizontal direction ($\eta_{\mathrm{or,hmin}}$), perpendicular to the maximum direction and representing the horizontal direction with the smallest fibre alignment. The two horizontal directions reflect the fibre influence on the flexural resistance of the slab. They can be interpreted as the two principal directions of fibre orientation within the horizontal plane. Appendix A includes additional information about the calculation of the fibre orientation factors, and explains the procedure used to determine the directions of maximum and minimum horizontal fibre alignment.

The spatial variation factor η_{sv} is smaller than 1.0 in most cases (16 out of 18 cores), indicating that the regions where the cores were extracted presented lower amounts of fibres than the nominal volume ratio, ρ_{f}. Their location in the slab plan, away from the lateral formworks and also not too close to the casting points (Fig. 2d-f), could explain these measurements, as according to [33], the highest fibre concentrations can be expected around the casting location and the lowest near the lateral formworks. The maximum horizontal fibre orientation factor $\eta_{\mathrm{or,hmax}}$ is always greater than 1.0, and typically presents values over 1.15. This indicates that, in all cores, there was a predominant fibre orientation in the horizontal plane. On the contrary, the vertical fibre orientation factor $\eta_{\mathrm{or,z}}$ is in most cases lower than 1.0, emphasising the preferential horizontal orientation of fibres (many researchers have observed similar results [27,31,33,35,37]). The minimum horizontal fibre orientation factor typically takes intermediate values between the other two, in many cases below 1.0. An exception to the trends can be observed in cores S125–0,5-SW and S125–0,5-SE, where the vertical fibre orientation factor has values higher than one. In the case of core S125–0,5-SW, the vertical orientation factor is higher than both the two horizontal factors. These results show that slab S125–0,5 presented the closest fibre distribution to an isotropic scenario, with differences between the three fibre orientation factors smaller than 20%. All other slabs presented a clear dominance of the horizontal fibre orientation. This was most notable in the 250 mm thick slabs, where very low values of the vertical fibre orientation factor $\eta_{\mathrm{or,z}}$ were measured, with a maximum of 0.79 in core S250–1,0-NW, and values lower than 0.63 in all remaining cores.

3.3. Analysis of fibre distribution and orientation

This section presents detailed results of the fibres' spatial distribution and orientation both for the full cores (Fig. 6) and in horizontal layer divisions (Fig. 7), as well as the spatial distribution of fibres through the thickness of the slabs. The possible ranges of straight fibre lengths (0÷35 mm, l_{f}), vertical orientations (0÷90°, angle β between the fibre and the horizontal plane) and horizontal orientations (0÷180°, angle φ between the fibre horizontal projection and scanning axis x) were discretised in intervals of fixed width (Δl, $\Delta\beta$, $\Delta\varphi$). They are presented in the graphs in the abscissa. The measured fibre volume ratios within a given interval $\Delta\rho_{\mathrm{f,meas}}$ are presented in the ordinate of the diagrams. The measured distributions of fibre vertical and horizontal orientations are compared with the theoretical values, which refer to an isotropic fibre orientation (see Appendix B for the derivation of the theoretical curves).

It is worth highlighting two specific aspects of the treatment of the fibre data to obtain the fibre orientation results. On one hand, detected fibres shorter than 3 mm (~9% of the straight fibre length) were removed from the orientation analyses. This fraction represented a very limited portion of the fibre content, so its influence on the overall results was negligible. Moreover, as reported in [31], very short fibres could correspond to the fibre hooks and hence not be representative of the actual orientation in space of the fibre axis. On the other hand, for the by-layer analysis (Fig. 7), fibres that crossed several layers were divided into segments to reflect the real fibre volume ratio in each layer. Regarding the orientation of each segment, the global fibre orientation (that of the fibre axis) was assigned to all the fibre segments. This procedure avoided the problem of having unreliable fibre orientations if, for instance, only the hook of the fibre belonged to one layer.

Fig. 6 shows the global fibre dispersion results for one selected core of each slab. Results of different cores from the same slab did not present significant variations. Thus, cores were selected based on the clarity of the trends and the quality of the reconstruction process. It is important to note that cores S68–1,0-SE, S125–0,5-NE, and S125–1,0-NW were analysed using the skeletonization technique, hence their results correspond to the portion of the cores from the slab bottom face to the level of the top reinforcement. Fig. 6a,c,e, and g correspond to the slabs with 0.5% nominal fibre volume ratio, while Fig. 6b,d,f,h correspond to slabs with 1.0% nominal fibre volume ratio.

Fig. 6a,b show the spatial distribution of fibres in the thickness of the slab by means of the spatial variation factor η_{sv}. The vertical axis has been normalised by the slab thickness to compare the trends for different slabs. Cores S68 had a higher concentration of fibres in the middle of the slab. This concentration of fibres could be caused by the reduced rebar spacing (70 mm, see Table 1) with respect to the fibre length, which could have forced fibres to accumulate between the two top rebar layers and altered the fresh concrete flow (please note that slabs S68 did not have bottom reinforcement). Cores S125 presented a lower volume of fibres below the top reinforcement. Cores S250 had several common features: (i) a lower volume of fibres below the top reinforcement (like cores S125); (ii) an increase of fibre volume between the top reinforcement and the top slab surface; and (iii) another concentration of fibres between 0.25 h and 0.4 h, also reported in [35]. Core S250–1,0-NW also had a higher fibre concentration near the bottom slab face.

Fig. 6c,d present the distribution of fibre projected lengths l_{f}. The majority of the fibre volume corresponded to full-length fibres even though there was a significant number of fibres that were shorter than the full length due to the core extraction process. Short-fibre volumes were more significant in some cores due to the predominantly horizontal

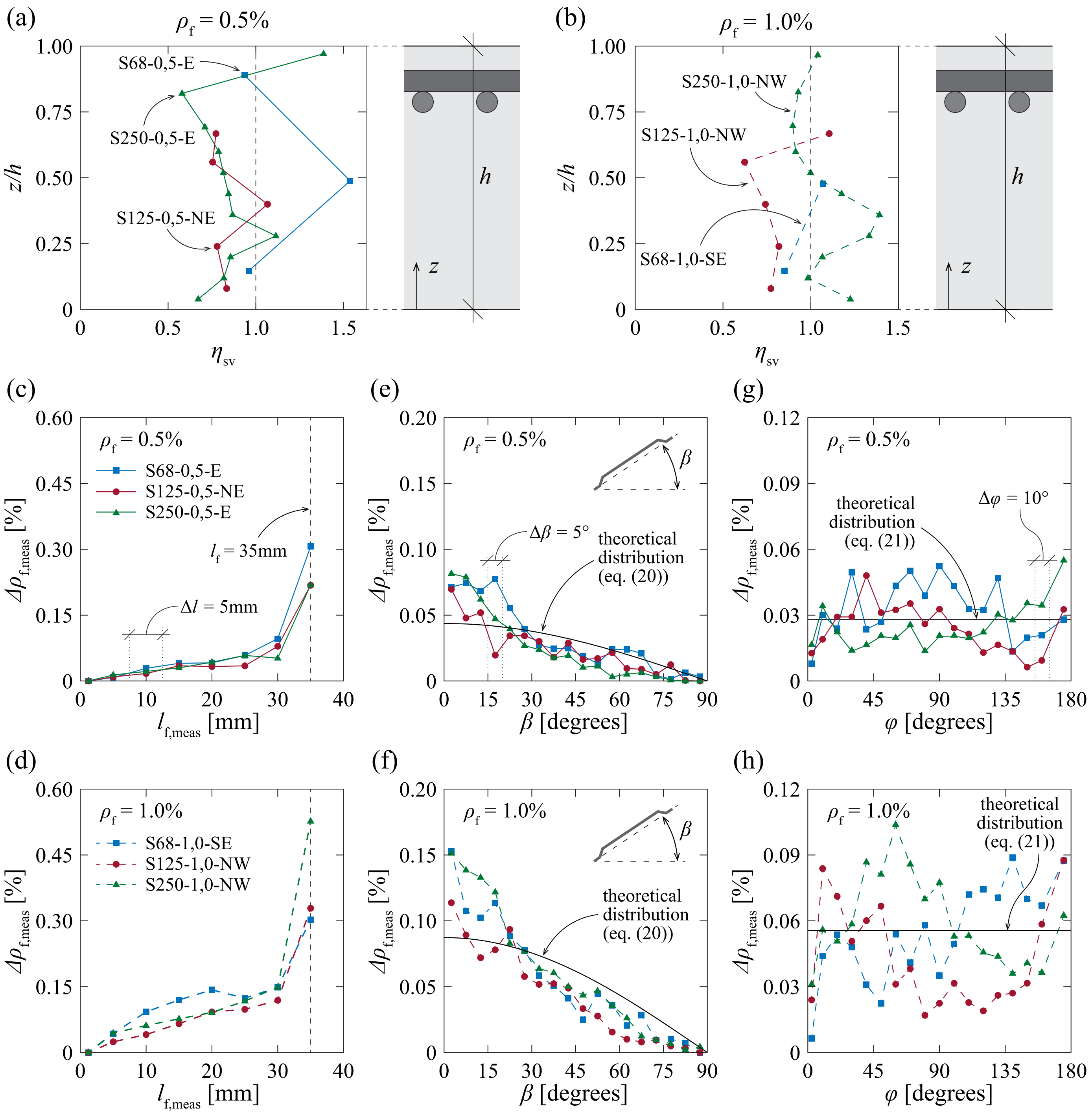

Fig. 6. Results of fibre spatial distribution and orientation for selected cores: fibre spatial distribution in the slab thickness for slabs with (a) 0.5% nominal fibre volume and (b) 1.0% nominal fibre volume; distribution of fibre lengths for slabs with (c) 0.5% fibre volume and (d) 1.0% fibre volume; distribution of fibre vertical orientations for slabs with (e) 0.5% fibre volume and (f) 1.0% fibre volume; and distribution of fibre horizontal orientations for slabs with (g) 0.5% fibre volume and (h) 1.0% fibre volume.

orientation of fibres, meaning that more fibres were cut during the core extraction. Fig. 6e,f compare the measured and theoretical (isotropic) distributions of fibre vertical orientations. It can be noticed that the flat or quasi-flat ($0 \div 25°$) fibre volumes were significantly higher than those corresponding (theoretically) to an isotropic distribution. On the other hand, pseudo-vertical fibre volumes were systematically lower than the theoretical values. Finally, Fig. 6g and h illustrate the measured and theoretical distributions of fibre horizontal orientations. An oscillation of the measured fibre volumes around the theoretical value can be clearly observed, most probably due to the influence of the flow of fresh concrete on the orientation of fibres, i.e., the relative position between the casting point and the core location [32–34,43,45]. The presence of the reinforcement layers could have also been a source of heterogeneity in the horizontal fibre orientation, impeding a free fibre flow (a similar effect was observed for tests with ρ_f equal to 0.5% and 1.0%).

Fig. 7 depicts the distribution of vertical fibre orientations for the selected cores at several horizontal layers (L1, L2, L3, and L4, see sketches on the top-right corner of each plot). The measurements are

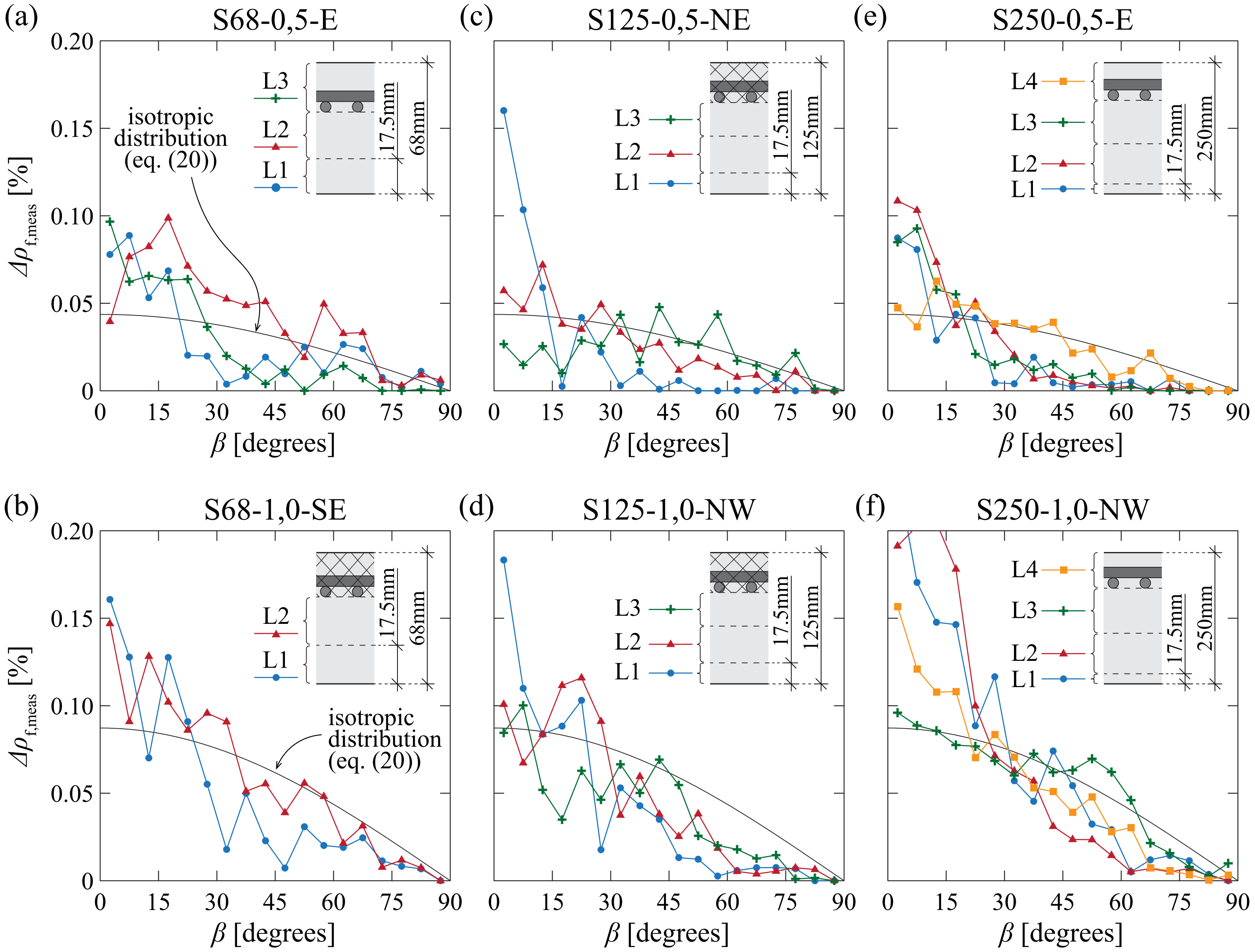

Fig. 7. Distributions of vertical fibre orientations by horizontal layers for selected cores: (a) S68–0,5-E; (b) S68–1,0-SE; (c) S125–0,5-NE; (d) S125–1,0-NW; (e) S250–0,5-E; and (f) S250–1,0-NW.

compared with the theoretical distribution (Eq. 20 of Appendix B) for the nominal fibre volume ratios of 0.5% and 1.0%, respectively. The bottom layer (L1) had a thickness of 17.5 mm in all cores (equal to $l_f/2$), and was aimed at analysing the influence of the wall effect of the bottom formwork on the fibre vertical orientation [28,33,35]. Another inter-layer division was set under the top reinforcement layers ($z = d_{top} - \O_{top}$, where z is the vertical distance measured from the slab bottom face, d_{top} the effective depth of the top reinforcement, and $\O_{top}$ the top layers' rebar diameter, see Fig. 2c), to isolate in a single layer the region between the top reinforcement and the top slab surface (layer L4 in slabs S250, and L3 in slabs S68). The space between these two extreme layers was divided into one (layer L2, slabs S68) or two layers (L2 and L3, slabs S125 and S250). In some cores, due to the use of the skeletonization reconstruction technique (see Section 2.2), the layer between the top flexural reinforcement and the top slab face was not analysed. For these cores, the corresponding layer has been hatched in the sketches of Fig. 7. This was the case of cores S68–1,0-SE, S125–0,5-NE, and S125–1,0-NW. Particularly, slabs S125 were all reconstructed using the skeletonization technique, so none of them included layer L4.

The results show two main trends:

1. The bottom layers typically presented very low fibre volumes with angles greater than 45°. Most of their fibre volume corresponded to flat angles (lower than 25°) [55,56]. Moreover, three cores presented a remarkable number of fibres with angles smaller than 15°, suggesting that the combined effect of the formwork and the bottom reinforcement bars forced fibres to be practically horizontal in that layer.
2. The two top layers generally showed a larger percentage of fibres at vertical angles. This supports the previous observation of the influence of the top rebars on the fibre orientation around them. In cores S68, layer L2 had the largest portion of quasi-vertical fibres, similarly to layer L3 in cores S125. In cores S250, both layers L3 and L4 reflected this effect, as the rebar interference did not only affect the layer directly below, but also the thickness occupied by the bars. While core S250-0,5-E had more pseudo-vertical fibres in the top layer L4, core S250-1,0-NW did so in layer L3.

4. Fibre effectiveness in punching and flexure

The measurements of fibre distribution and orientation in the six SFRC slabs indicate that the actual orientation of steel fibres was not isotropic but tended to be horizontal. This deviation can be attributed to the flow of fresh concrete [30,32–34,43,45,46], the interference of the rebars, and the wall effects caused by the formwork [28,33,35]. These findings suggest that the transfer of shear forces through inclined cracks was smaller than that of an isotropic distribution of fibres in the volume. Similarly, the horizontal transfer of forces through vertical cracks was

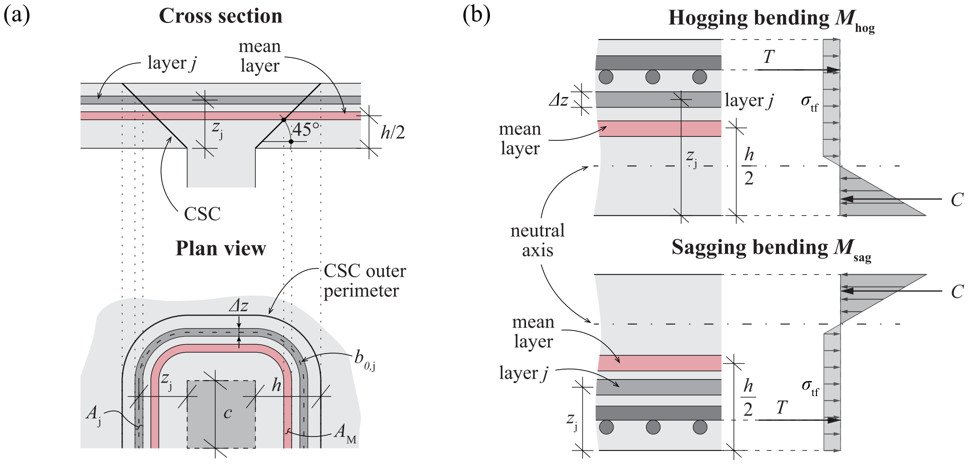

Fig. 8. Slab division in horizontal layers to consider the fibres effectiveness as a function of their vertical position: (a) in punching; and (b) in flexure.

higher than in an isotropic scenario. Therefore, fibres in these slabs had a lower degree of efficiency in enhancing punching than flexure. Furthermore, the spatial distribution of fibres and their orientation were not uniform through the slab thickness. Consequently, different layers within the slab had variable degrees of effectiveness in enhancing punching and flexure. For instance, fibres near the slab top face were more efficient in enhancing hogging bending moments, while fibres near the slab bottom face were more effective in improving sagging moments.

Based on these findings, the averaged orientation factors ($\eta_{or,\alpha}$) for the full slab thickness (as done in Section 3.2) may not be completely representative of the actual enhancement of a slab's punching and flexural resistances. The division of a slab in horizontal layers allows accounting for the contribution of each slab slice separately. By defining layer effectiveness factors for punching and flexure ($k_{eff,j}$), we establish the relative efficiency of the fibres in each slice with respect to the contribution of the average slice in punching and flexure. The combination of these layer effectiveness factors with the orientation factors (computed for each layer) provides a better estimation of the actual overall fibre contribution to the punching and flexural resistances.

4.1. Definition of global and layer effectiveness factors

Fig. 8 depicts the variable effectiveness of fibres at different layers in enhancing punching and flexure. Fig. 8a illustrates this concept for punching in cross section (top) and plan view (bottom). In the context of the Critical Shear Crack Theory (CSCT, [6]), a Critical Shear Crack (CSC, see Fig. 8a) governs the resistance of the connection. It originates from a flexural crack at the slab top face, and propagates towards the column face at an angle of approximately 45°, hence having roughly a truncated conical shape. This crack geometry implies that the vertical fibres in upper slab layers contribute more to the punching resistance than the vertical fibres near the bottom slab face, as their tributary areas A_j are larger.

Fig. 8b, on the other hand, depicts the variable effectiveness of fibres in increasing the cross-sectional flexural capacity, both for hogging (top) and sagging (bottom) bending moments. Layers on the tensile side of the slab and farther away from its neutral axis have a larger contribution to the cross-sectional flexural resistance thanks to an increased lever arm.

Following the approach of the fibre orientation ($\eta_{or,\alpha}$) and spatial variation (η_{sv}) factors, and dividing the slab thickness in layers, global punching (η_V) and flexural (η_M) effectiveness factors can be defined. The general expression of the global effectiveness factor η_{eff} is defined by Eq. (4). Assuming a division of the slab thickness in n_j layers, the global effectiveness factor (η_{eff}) is defined as the product of the fibre orientation factor of each layer in the desired direction α ($\eta_{or,\alpha,j}$) by the corresponding layer effectiveness factor ($k_{eff,j}$), summed for all layers. These layer effectiveness factors can be defined for punching ($k_{V,j}$, Eq. (5)), for hogging moments ($k_{Mhog,j}$, Eq. (6)), and for sagging moments ($k_{Msag,j}$, Eq. (7)).

$$\eta_{eff} = \sum_{j=1}^{n_j} \left(k_{eff,j} \cdot \eta_{or,\alpha,j} \right) \tag{4}$$

$$k_{V,j} = \frac{b_{0,j}}{4c + \pi h} \tag{5}$$

$$k_{Mhog,j} = \frac{z_j}{h/2} \tag{6}$$

$$k_{Msag,j} = \frac{h - z_j}{h/2} \tag{7}$$

where the variables used in this formulation are defined in Fig. 8. The generic direction α corresponds to the vertical direction z for the punching layer effectiveness factor $k_{V,j}$ and to the horizontal directions of maximum and minimum fibre alignment, considered for the full core height, for the hogging and sagging flexural layer effectiveness factors $k_{Mhog,j}$ and $k_{Msag,j}$. For the flexural verification of slabs, considering the mean of the maximum and minimum effectiveness factors seems adequate, as the yield lines cross several zones with different predominant fibre orientations. An exception is represented by narrow one-way slabs, where the governing fibre orientation should be considered. For the verification of flat slabs around the column region, the consideration of the average of the minimum and maximum directions is again a reasonable assumption, since the radial and tangential moments are involved in the mechanism. The derivation of the layer effectiveness factors is presented in Appendix A.

It has to be noted that vertical fibres can carry directly a portion of the shear force around the column. Therefore, the global effectiveness factor for the punching shear resistance (η_V) will account for the orientation factor in vertical direction ($\eta_{or,z}$), weighted by the length of the layer perimeter, as shown above. Furthermore, as demonstrated by the Critical Shear Crack Theory (CSCT), the flexural stiffness and the hogging flexural resistance determine the local deformation of the slab around the column and particularly the opening of the Critical Shear Crack (CSC) at failure. This opening is a key factor influencing the capacity of concrete to carry shear forces across the CSC [6,13].

Consequently, when the fibres are mostly vertically oriented, the flexural deformation is higher ($\eta_{\text{Mhog}} < 1.0$) and the shear force carried by concrete is lower, whereas the shear force carried directly by the fibres is higher ($\eta_{\text{V}} > 1.0$) than for the case of isotropically-oriented fibres ($\eta_{\text{Mhog}} = \eta_{\text{V}} = 1.0$). The shear enhancement by the fibres is thus less than proportional to the effectiveness factor η_{V} described above (see point A in Fig. 9). On the contrary, in the case of mostly horizontally-oriented fibres ($\eta_{\text{Mhog}} > 1.0$), the opening of the CSC is smaller and the shear force carried by concrete increases, which partially compensates the lower direct contribution of the vertically-oriented fibres ($\eta_{\text{V}} < 1.0$). Here again, the punching shear enhancement is less than proportional to the effectiveness factor η_{Mhog} described above (see point B in Fig. 9).

Nevertheless, the opening of the CSC and thus the concrete contribution to carry the shear force depend not only on the fibres, but also on the amount of flexural reinforcement, the concrete strength, the aggregate size, the effective depth (size effect) and the column size. This means that is it not possible to define all these effects with a constant effectiveness factor for punching shear. For this reason, the global effectiveness factor for punching η_{V} is defined in a simplified manner accounting only for the spatial variation and the orientation of the fibres.

4.2. Application to the slabs under study

Based on this simplification, the punching and flexural global effectiveness factors can be calculated for the slabs under analysis according to the following procedure. In a first step, the fibre orientation factors along the vertical and horizontal directions with maximum and minimum fibre alignment are calculated for the layers defined in Fig. 7. The directions of maximum and minimum horizontal fibre alignment are fixed for each core and equal to those obtained in the global core orientation analyses (see Fig. 13 in Appendix A). The results are presented in Fig. 10 for the six cores analysed in Figs. 6 and 7. In the abscissa, the orientation factor in each layer has been normalised by the ratio $h_{\text{core}}/\Delta z_{\text{j}}$. This is necessary to make results of different layers comparable, due to the variable layer thickness. In the ordinate, the ratio of the layer height to the slab thickness is represented. Fig. 10c, f, and i show schematically the cross section of the different slabs, with the position of the flexural reinforcement and the layer division (for cores S68–1,0-SE, S125–0,5-NE and S125–1,0-NW, the fibres in the upper slab portion were not reconstructed, see hatched area in Fig. 10f and Section 2.2).

The layer representation of the fibre orientation factors shows the variation of the fibre alignment inside the slab along the vertical direction. The vertical fibre orientation factor ($\eta_{\text{or,z}}$) is higher in the layer right below the top flexural reinforcement in most cores. This is in agreement with the observations of the fibre orientation by layers (Fig. 7). An exception to this is core S250–0,5-E, in which the largest value of the vertical fibre orientation factor is at the top layer (layer L4, Fig. 10g). It should be noted that this core did not intercept top bars; therefore, the flexural rebars could have had a lesser influence at this location. The vertical orientation factor is systematically lower in the bottom layer, showing the effect of the formwork. The maximum horizontal fibre orientation factor ($\eta_{\text{or,hmax}}$) takes similar values at the top and bottom layers in cores S250–1,0-NW and S68–0,5-E, yet the distribution in the intermediate layers is rather variable. The minimum horizontal fibre orientation factor ($\eta_{\text{or,hmin}}$) sometimes takes higher values than the maximum. This is due to the fact that the maximum and minimum directions are considered for the complete cores and not per layer.

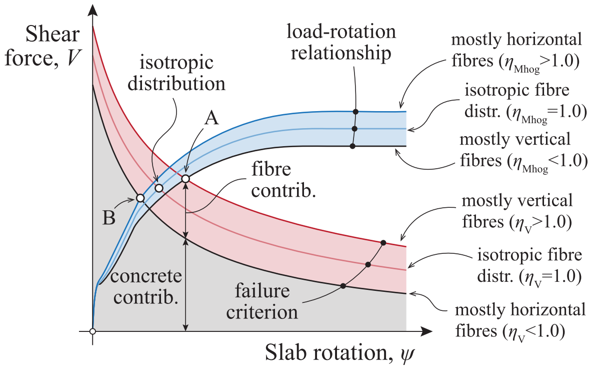

Fig. 9. Application of the Critical Shear Crack Theory to the punching resistance of SFRC slabs according to [13] (circles indicate the punching shear resistance and the rotation at failure for three cases: mostly vertically-oriented fibres (point A); mostly horizontally-oriented fibres (point B); and isotropic distribution of fibres (intermediate point)).

The complete results of the fibre orientation factors are included in Table 3, where the mean value and standard deviation have been calculated for each slab. These average slab results and their scatter are presented in Fig. 11a for the slabs with 0.5% nominal fibre volume ratio, and in Fig. 11b for the slabs with 1.0% nominal fibre volume ratio. The dispersion of results is rather small for slab S250–0,5, where the minimum horizontal orientation factor represents approximately an isotropic scenario. The maximum horizontal factor takes the highest value in all slabs, and the vertical orientation factor is the smallest in almost all slabs. In slab S68–0,5, the vertical and minimum horizontal factors are both close to an isotropic distribution, yet a clearly governing fibre alignment is indicated by the maximum horizontal direction factor. Interestingly, slab S125–0,5 presents an average vertical orientation factor equal to the isotropic case, with a value of 1.10 in core S125–0,5-SW. It presents the lowest values for both the maximum and minimum horizontal orientation factors of all slabs.

The results of the slabs with 1.0% fibre volume ratio show in general smaller scatter. The minimum horizontal factor is very similar for all slabs and almost equal to the isotropic scenario. The vertical fibre orientation factor is always smaller than either of the horizontal factors. It shows a clear descending trend for thicker slabs, and it is generally smaller for cores with 1.0% nominal fibre volume ratio than with 0.5%. This observation suggests that both the increase in slab thickness and in fibre content are detrimental to the fibre effectiveness in the vertical direction. The maximum horizontal factor is also similar for all three slabs, with no clear trend for increasing slab thicknesses.

Fig. 11c,d show the punching and flexural global effectiveness factors for the slabs with 0.5% and 1.0% nominal fibre volume ratio, respectively. The results are also presented in Table 4, see Appendix C. It is worth noting that, when computing the layer effectiveness factors, the slab depth was replaced by the reconstructed core height in Eqs. (14), (15) and (16), see Appendix A. For the minimum hogging ($\eta_{\text{Mhog,min}}$) and sagging ($\eta_{\text{Msag,min}}$) global effectiveness factors, the results are very similar to the minimum horizontal fibre orientation factor in all slabs. This is expected, as the average values of the minimum horizontal orientation factor are very similar to an isotropic scenario in all slabs. The global punching effectiveness factor (η_{V}) gives very similar values to those of the vertical orientation factor; the scatter of the results is also comparable.

In the maximum hogging ($\eta_{\text{Mhog,max}}$) and sagging ($\eta_{\text{Msag,max}}$) global effectiveness factors, the variability of results is larger. For slabs S68, where two cores out of six were reconstructed in their full thickness, the sagging effectiveness factor is slightly larger than the hogging one. The fact that not all cores were reconstructed in their full height increases the scatter of results. This difference between factors is significantly higher in slabs S125, where all cores were only reconstructed up to the level of the top flexural reinforcement. For all cores in which the region between the top rebars and the upper slab face was not reconstructed, fibres in the lower layers are significantly flatter than in upper layers, where more fibres are oriented vertically (see Fig. 10b,d,e). A direct consequence of this is a better disposition of fibres for enhancing the sagging

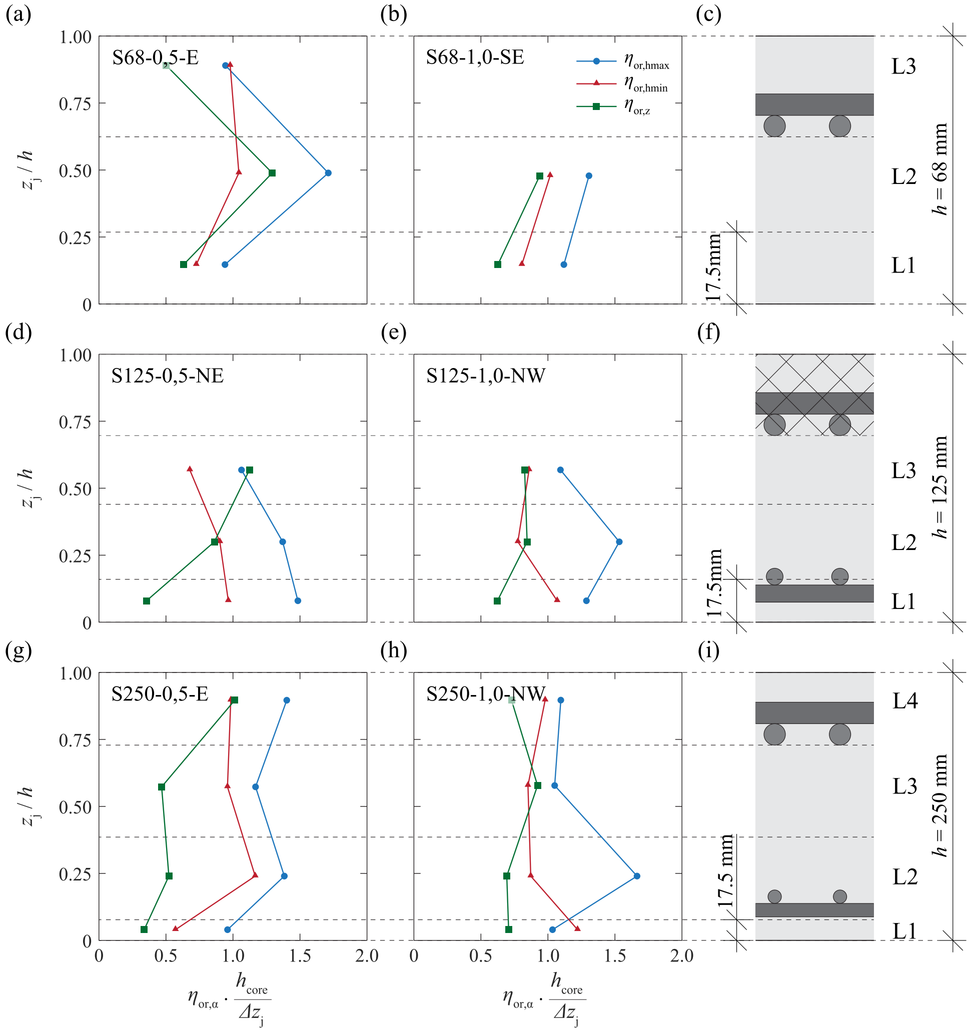

Fig. 10. Variation of normalised fibre orientation factors along the slab thickness for selected cores: (a) S68–0,5-E; (b) S68–1,0-SE; (c) layer division in slabs S68; (d) S125–0,5-NE; (e) S125–1,0-NW; (f) layer division in slabs S125; (g) S250–0,5-E; (h) S250–1,0-NW; (i) layer division in slabs S250.

flexural capacity than the hogging one. The fact that the difference between the maximum hogging and sagging effectiveness factors is higher for slabs S125 than S68 is explained by a larger portion of cores not reconstructed in their full height. In slabs S250, the average values of the hogging and sagging global effectiveness factors are similar, as most cores were reconstructed in full. The scatter in the global effectiveness factors is overall higher than in the fibre orientation factors. The spatial distribution and orientation of fibres within the slab thickness presents some general trends, but vary between the different cores in a slab. The global effectiveness factors emphasise this heterogeneity due to the introduction of each layer's effectiveness in punching and flexure. The differences in fibre orientation between cores are thus evidenced by the layer effectiveness factors, which can explain the observed larger scatter.

5. Conclusions

This paper deals with the distribution and orientation of steel fibres in reinforced concrete slabs with conventional steel reinforcement, and their influence on punching and flexural behaviour. The extraction of cores from SFRC slabs for their scanning using micro-Computed Tomography allowed evaluating the actual fibre distribution in the specimens. The spatial distribution and orientation of the fibres were analysed, both for the full cores and dividing them in horizontal layers. Fibre spatial variation and orientation, as well as shear and flexural effectiveness factors, have been defined and computed to evaluate the impact of the measured fibre dispersion and orientation on the slabs' flexural and punching resistances. The main concluding remarks are summarised in the following:

1. Fibre spatial distribution and orientation are strongly affected by the presence of the flexural reinforcement. In flat slabs, with rebars arranged in orthogonal layers, the clear space between bars plays an important role, with a greater influence for smaller rebar spacings. Below rebar crossings, fibre content tends to be smaller.
2. The flowability of fresh concrete and the distance to be covered by fibres between the casting point and their final position in the structural element have a significant influence on the fibre spatial distribution and orientation in flat slabs. Due to their larger dimensions, 250 mm thick specimens show a flatter fibre orientation than specimens 68 mm thick, which in principle would be expected to exhibit stronger wall effects.

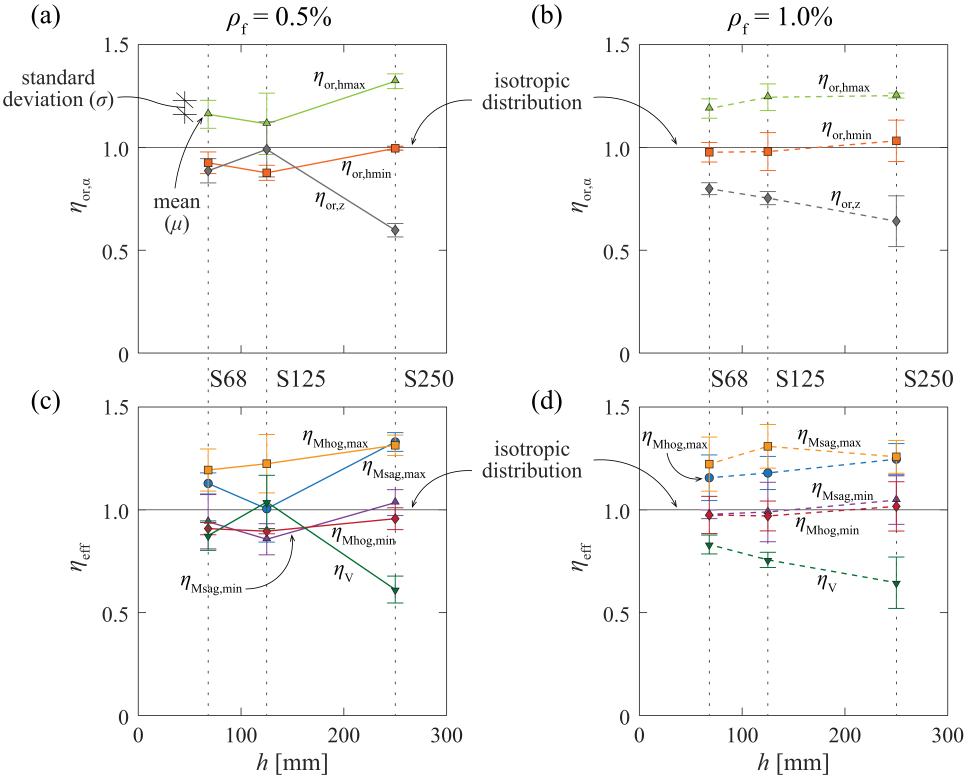

Fig. 11. Influence of slab thickness and fibre dosage on the fibre orientation: average fibre orientation factors for slabs with (a) 0.5% fibre volume ratio and (b) 1.0% fibre volume ratio; average effectiveness factors for slabs with (c) 0.5% fibre volume ratio and (d) 1.0% fibre volume ratio (the reader is referred to the online paper version for the colour codes).

3. Fibres present flatter orientations near the top and bottom slab surfaces. On the contrary, the region at the level of the top flexural reinforcement and right below it exhibits the largest proportion of vertical fibres.
4. An increase in fibre dosage leads to a greater predominance of horizontally-oriented fibres, probably related to the use of higher amounts of superplasticizer.
5. Even in slabs with quasi-horizontal fibre arrangements, there is a predominant direction in which fibres tend to align the most. Fibres do not tend to orient uniformly in 2D, but have two principal directions, influenced by the concrete flow and the flexural reinforcement.
6. The orientation of fibres is typically flatter than in an isotropic scenario. For the punching resistance of flat slabs, this implies that the enhancement of the load-carrying capacity due to the shear force carried directly by the fibres is limited. At the same time, their contribution is more significant in reducing the flexural deformations of the slab, with an increase of the shear forces transferred by the concrete through aggregate interlocking.

Since the presence of flexural reinforcement affects the orientation and distribution of fibres, the findings of this work cannot be generalised to slabs without conventional reinforcement. In addition, non-metallic fibres can potentially behave differently, limiting the generalisation for this case as well. These two scenarios deserve to be investigated in further research.

CRediT authorship contribution statement

Diego Hernández Fraile : Conceptualization, Methodology, Validation, Formal analysis, Investigation, Data curation, Visualization, Writing – original draft. **Enrico Faccin:** Conceptualization, Methodology, Investigation, Writing – review & editing. **Fausto Minelli:** Conceptualization, Writing – review & editing, Supervision, Project administration. **Giovanni Plizzari:** Conceptualization, Writing – review & editing, Supervision, Project administration. **Aurelio Muttoni:** Conceptualization, Methodology, Formal analysis, Writing – review & editing, Supervision, Project administration.

Declaration of Competing Interest

The authors declare that they have no known competing financial interests or personal relationships that could have appeared to influence the work reported in this paper.

Data availability

Data will be made available on request.

Acknowledgements

The authors would like to express their gratitude to the Interdisciplinary Platform for X-ray micro-tomography (PIXE) of EPFL, especially to Albert Taureg and Gary Perrenoud, who performed the CT-scans of the concrete cores and provided technical support in the core reconstruction. The authors would also like to acknowledge the contribution of EPFL Master Students Luc Alberti, Joëlle Lu and Alexis Talla Simo, who helped in the 3D reconstruction of the concrete cores with software Avizo, and of UNIBS Master Students Luca Spinelli and Luca Tognassi for their contribution in the core extraction.

Appendix A. Derivation of fibre orientation and fibre effectiveness factors

Eq. (2) provides the general definition of the measured effective fibre volume ratio in a generic direction α. The fibre orientation angles β_{i} and φ_{i} obtained from the core reconstruction allow projecting the fibre along the three axes defined in this paper. The corresponding fibre orientation factors can be calculated with Eq. (8) for the vertical direction ($\eta_{\mathrm{or,z}}$), with Eq. (9) for the horizontal direction with maximum fibre alignment ($\eta_{\mathrm{or,hmax}}$), and with Eq. (10) for the horizontal direction with minimum fibre alignment ($\eta_{\mathrm{or,hmin}}$).

$$\eta_{or,z} = 2\cdot\frac{\sum_{i=1}^{n_i}\left(l_{f,dev,i}\cdot \sin\beta_i\right)}{\sum_{i=1}^{n_i} l_{f,dev,i}} \tag{8}$$

$$\eta_{or,h\ \max} = 2\cdot\frac{\sum_{i=1}^{n_i}\left(l_{f,dev,i}\cdot \cos\beta_i\cdot \cos\left(\varphi_i-\varphi_{0,\ \max}\right)\right)}{\sum_{i=1}^{n_i} l_{f,dev,i}} \tag{9}$$

$$\eta_{or,h\ \min} = 2\cdot\frac{\sum_{i=1}^{n_i}\left(l_{f,dev,i}\cdot \cos\beta_i\cdot \cos\left(\varphi_i-\varphi_{0,\ \min}\right)\right)}{\sum_{i=1}^{n_i} l_{f,dev,i}} \tag{10}$$

Angles $\varphi_{0,\max}$ and $\varphi_{0,\min}$ correspond to the angles between axis x in the CT-scan and the directions where fibre alignment is maximum and minimum, respectively. These axes have been calculated following a numerical procedure, presented in Fig. 12. From Fig. 6g and h, one can observe that the fibre volume ratio with respect to angle φ oscillates around the theoretical isotropic value. For instance, the results of core S250–1,0-NW show a distribution with a maximum at $\varphi \approx 55^\circ$ and a minimum at $\varphi \approx 145^\circ$, hence orthogonal between them. Defining an angle φ_0 that represents the rotation of a fictitious axis x' with respect to axis x of the CT-scan (Fig. 12a), the fibre orientation factor along that direction $\eta_{\mathrm{or},x'}$ can be computed with Eq. (11). By varying angle φ_0 in the range $0\div180^\circ$, one obtains the fibre orientation factor for direction x' as a function of φ_0. Fig. 12b shows these results for core S125–0,5-NE. From this calculation, one can extract the maximum and minimum values of the fibre orientation factor, which are included in Table 3. The corresponding orientations can also be obtained, indicated by angles $\varphi_{0,\max}$ and $\varphi_{0,\min}$ defined in Fig. 12b and used in Eqs. (9) and (10).

$$\eta_{or,x'} = 2\cdot\frac{\sum_{i=1}^{n_i}\left(l_{f,dev,i}\cdot \cos\beta_i\cdot \cos\left(\varphi_i-\varphi_0\right)\right)}{\sum_{i=1}^{n_i} l_{f,dev,i}} \tag{11}$$

Since the direction of axes x and y in the CT-scans do not correspond with the axes of the slabs, it was not possible to link the local core axes x and y to the axes of the slab specimens. For this reason, the directions of maximum and minimum horizontal fibre alignment have been defined in this appendix, and used throughout the paper.

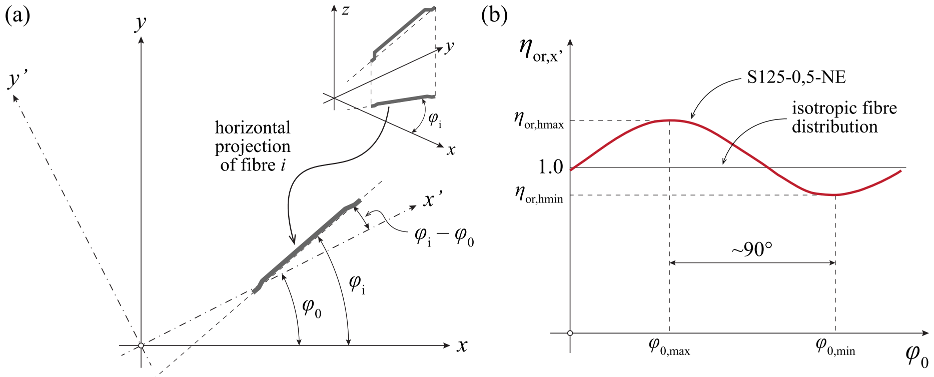

Fig. 12. Directions of minimum and maximum horizontal fibre orientation: (a) definition of direction x′ and the corresponding angles; (b) results of the numerical procedure for core S125–0,5-NE.

.

Fig. 13 shows the horizontal orientation analysis for all cores. Cores with a smaller difference between the minimum and maximum values of $\eta_{\mathrm{or},x'}$ correspond to scenarios with a more uniform fibre distribution in the horizontal plane. Usually, the mean values of the maximum and minimum directions are higher that 1.0 (isotropic case) since the fibres are predominantly in horizontal planes.

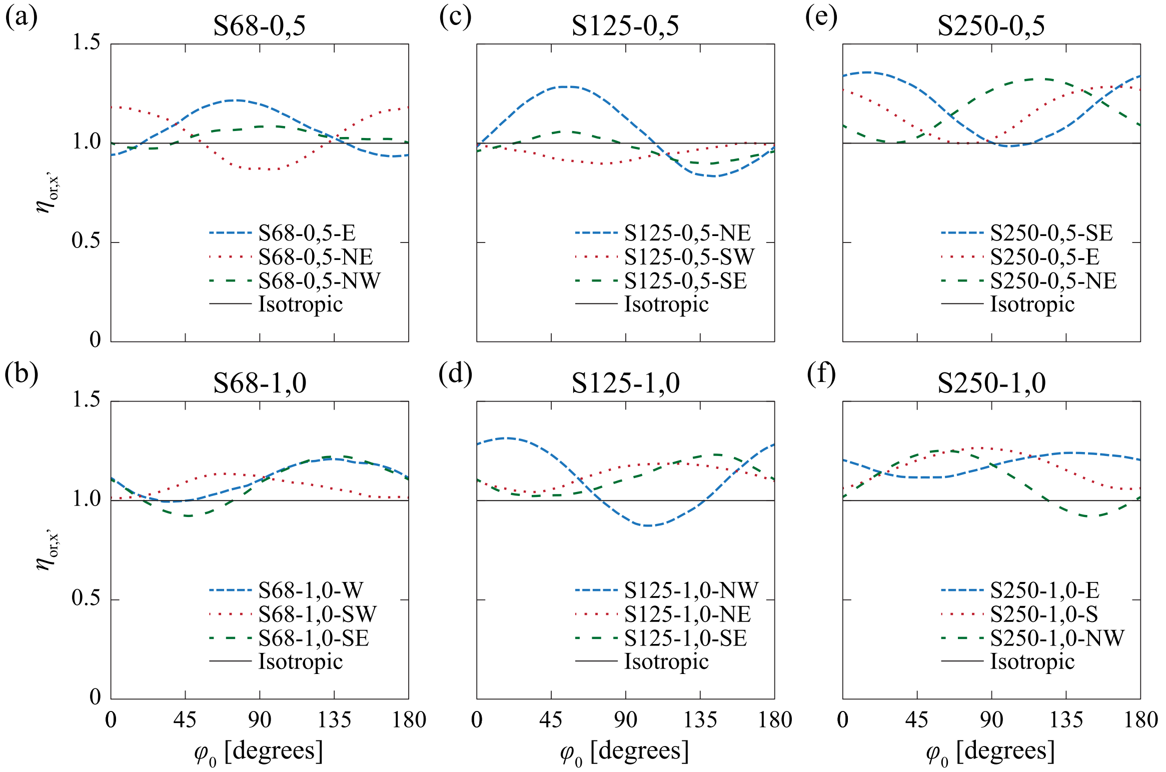

Fig. 13. Calculation of the directions of minimum and maximum horizontal fibre orientation for all slabs: (a) S68–0,5; (b) S68–1,0; (c) S125–0,5; (d) S125–1,0; (e) S250–0,5; and (f) S250–1,0 (the reader is referred to the online paper version for the colour codes).

.

The global effectiveness factors η_{eff} are based on the concept of the fibre orientation factors $\eta_{or,\alpha}$, which are adapted to consider the variability of the fibre spatial distribution and orientation within the slab thickness, plus the effectiveness of the fibres of a given layer in transferring punching shear or flexure. The reader is referred to Fig. 8 for the definition of layers and all parameters involved in this derivation.

The contribution of the fibres in layer *j* to the punching resistance of the connection, $V_{R,f,j}$, results from the product of the horizontal projection of the surface of the Critical Shear Crack (CSC) within that layer, A_j, times the residual tensile stress, $\sigma_{tf,j}$.

$$V_{R,f,j} = A_j \cdot \sigma_{tf,j} \tag{12}$$

If we assume that the residual tensile stresses are uniform along the CSC and equal to a reference value σ_{tf}, [13], then the ratio of the contributions of two layers *j* and *k* is

$$\frac{V_{R,f,j}}{V_{R,f,k}} = \frac{A_j \cdot \sigma_{tf,j}}{A_k \cdot \sigma_{tf,k}} = \frac{A_j}{A_k} \tag{13}$$

If layer *k* is taken as the layer with the average contribution in the slab, then Eq. (13) corresponds to the contribution of layer *j* relative to the average contribution along the CSC. The average layer corresponds to the layer at the slab's mid-height ($z_k = h/2$), and is referred to as the mean layer, see Fig. 8a. Eq. (13) with layer *k* substituted by the mean layer provides the weighing factor for the vertical fibre contribution of layer *j* in punching relative to the average contribution along the CSC. This ratio results in the punching shear effectiveness factor of layer *j* $k_{V,j}$, as defined in Eq. (5). Parameter $b_{0,j}$ is the punching control perimeter of layer *j*, according to the formulation of Model Code 2010 [1] and the draft of the new generation of Eurocode 2 [2].

$$k_{V,j} = \frac{A_j}{A_M} = \frac{(4c + 2\pi z_j)\cdot \Delta z}{(4c + \pi h)\cdot \Delta z} = \frac{4c + 2\pi z_j}{4c + \pi h} = \frac{b_{0,j}}{4c + \pi h} \tag{14}$$

The contribution of fibres in layer *j* to the flexural resistance of the cross section can be evaluated with the increase in the bending moment due to the residual tensile stresses at that layer, $\Delta m_{f,j}$. Following the same rationale as for the punching shear effectiveness factor, if the increase of bending moment is computed with respect to the most compressed fibre of the cross-section (lever arm equal to z_j for hogging and $h - z_j$ for sagging), we obtain the hogging ($k_{Mhog,j}$, Eqs. (6) and (15)) and sagging ($k_{Msag,j}$, Eqs. (7) and (16)) effectiveness factors of that layer.

$$k_{Mhog,j} = \frac{\Delta m_{f,hog,j}}{\Delta m_{f,hog,M}} = \frac{z_j}{h/2} \tag{15}$$

$$k_{Msag,j} = \frac{\Delta m_{f,sag,j}}{\Delta m_{f,sag,M}} = \frac{h - z_j}{h/2} \tag{16}$$

Appendix B. Theoretical expressions for fibre orientation formulae

Fig. 14 illustrates the principle for computing the theoretical distribution of vertical fibre orientations, indicated by the angle between the fibre axis and the horizontal plane (β). All the possible positions of the fibre tips describe a sphere of radius $l_f/2$, with its centre at the fibre centre of gravity; the fibre angle with the horizontal plane can in general be defined as β_i. Taking only the upper half of the sphere, all the fibre orientations that would form an angle with the horizontal plane equal to β have their upper end contained in the area dA, marked in grey. Therefore, if we consider a uniform probability of a fibre to be oriented in any direction, the probability of a fibre to form an angle β with the horizontal plane can be expressed as the ratio of area dA to the total area of the top half spere $A_{1/2}$.

$$p\left(\beta_i = \beta\right) = \frac{dA}{A_{1/2}} \tag{17}$$

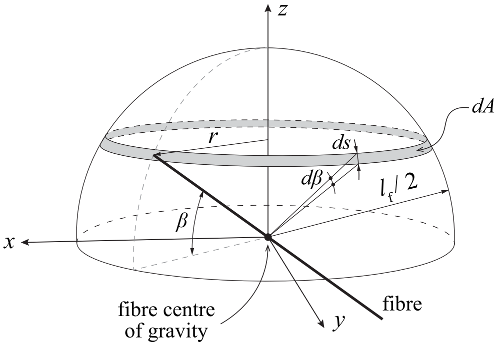

Fig. 14. Definition of variables for the theoretical distribution of vertical fibre orientations.

.

The expression for dA is

$$dA = 2\pi r \cdot ds \tag{18}$$

where $r = l_f/2 \cdot \cos(\beta)$ is the radius of the horizontal circumference described by the fibre tip, and $ds = l_f/2 \cdot d\beta$ is the width of area dA. Knowing that the area of half a sphere is $A_{1/2} = \pi \cdot l_f^2/2$, we obtain Eq. (19), which is the probability density function of the vertical fibre orientations:

$$p\left(\beta_i = \beta\right) = \frac{dA}{A_{1/2}} = \frac{2\pi \cdot l_f/2 \cdot \cos\beta \cdot l_f/2 \cdot d\beta}{\pi \cdot {l_f}^2/2} = \cos\beta \cdot d\beta \tag{19}$$

The same result was reached by Aveston and Kelly [14] (see also [39–42]).

This probabilistic approach can be used to develop an expression for the theoretical distribution of the vertical fibre orientations in a concrete volume. The range of β is $0 \div \pi/2$ and can be discretised in intervals of value $\Delta\beta$, which substitutes $d\beta$ in Eq. (19). The integral of Eq. (19) in the range $0 \div \pi/2$ is equal to 1.0, as it is by definition the cumulative distribution function of variable β in its full range of validity. To convert these expressions from probabilities of occurrence into fibre volume ratios, Eq. (19) has to be multiplied by the measured fibre volume ratio, $\rho_{f,meas}$. The resulting theoretical distribution corresponds to Eq. (20).

$$\Delta\rho_{f,\beta} = \rho_{f,meas} \cdot \cos\beta \cdot \Delta\beta \tag{20}$$

For the theoretical distribution of fibre horizontal orientations, the probability of the horizontal projection of a fibre to form an angle φ with axis x is constant and given by Eq. (21) for an interval $\Delta\varphi$ of 10° (value used in this paper).

$$\Delta\rho_{f,\varphi} = \rho_f \cdot \frac{\Delta\varphi}{\varphi_{\max} - \varphi_{\min}} = \rho_f \cdot \frac{10^\circ}{180^\circ} \approx 0.056 \cdot \rho_f \tag{21}$$

Appendix C. Results of flexural and punching effectiveness factors

Table 4
Flexural and punching global effectiveness factors.

Core	$\eta_{Mhog,max}$	$\eta_{Mhog,min}$	$\eta_{Msag,max}$	$\eta_{Msag,min}$	η_V
S68-0,5-E	1.19	0.98	1.24	0.89	0.79
S68-0,5-NE	1.10	0.79	1.26	0.94	0.92
S68-0,5-NW	1.09	1.05	1.08	0.90	0.91
Average (μ)	1.13	0.94	1.19	0.91	0.87
St. Dev (σ)	0.051	0.132	0.102	0.030	0.072
S68-1,0-W	1.05	0.96	1.37	1.03	0.79
S68-1,0-SW	1.15	1.00	1.12	1.02	0.88
S68-1,0-SE	1.27	0.97	1.18	0.87	0.83

(*continued on next page*)

Table 4 (*continued*)

Core	$\eta_{Mhog,max}$	$\eta_{Mhog,min}$	$\eta_{Msag,max}$	$\eta_{Msag,min}$	η_V
Average (μ)	1.16	0.98	1.22	0.97	0.83
St. Dev (σ)	0.111	0.021	0.132	0.091	0.046
S125-0,5-NE	1.19	0.77	1.38	0.90	0.89
S125-0,5-SW	0.91	0.89	1.09	0.91	1.14
S125-0,5-SE	0.91	0.91	1.20	0.88	1.08
Average (μ)	1.01	0.86	1.22	0.90	1.04
St. Dev (σ)	0.162	0.076	0.142	0.013	0.130
S125-1,0-NW	1.26	0.84	1.37	0.91	0.80
S125-1,0-NE	1.19	1.13	1.19	0.96	0.74
S125-1,0-SE	1.09	1.00	1.37	1.05	0.73
Average (μ)	1.18	0.99	1.31	0.97	0.76
St. Dev (σ)	0.081	0.145	0.106	0.073	0.037
S250-0,5-SE	1.38	1.00	1.33	0.97	0.55
S250-0,5-E	1.31	1.00	1.26	1.00	0.68
S250-0,5-NE	1.30	1.11	1.35	0.90	0.61
Average (μ)	1.33	1.03	1.31	0.96	0.61
St. Dev (σ)	0.046	0.063	0.049	0.053	0.065
S250-1,0-E	1.30	1.08	1.18	1.15	0.56
S250-1,0-S	1.28	1.14	1.25	0.97	0.59
S250-1,0-NW	1.16	0.92	1.34	0.93	0.79
Average (μ)	1.25	1.05	1.26	1.02	0.65
St. Dev (σ)	0.076	0.118	0.080	0.120	0.125

References

[1] fib, fib Model Code for Concrete Structures 2010, Ernst & Sohn, Berlin, Germany, 2013.

[2] Eurocode 2, 2023. Design of concrete structures - Part 1–1: General rules and rules for buildings, bridges and civil engineering structures, Final draft FprEN 1992–1-1, European Committee for Standardization (CEN), 405 p., Brussels, Belgium.

[3] Voo J.Y.L., Foster S.J., 2003. Variable engagement model for fiber reinforced concrete in tension, Australia.

[4] Ng T.S., Htut T.N.S., Foster S.J., 2012. Fracture of steel fibre reinforced concrete – The unified variable engagement model, School of Civil and Environmental Engineering, The University of New South Wales, R-406, Sydney.

[5] Kinnunen S., Nylander H., 1960. Punching of Concrete Slabs Without Shear Reinforcement, Transactions of the Royal Institute of Technology, N° 158, 112 p., Stockholm, Sweden.

[6] Muttoni A. Punching shear strength of reinforced concrete slabs without transverse reinforcement. Acids Struct J 2008;105(N° 4):440–50 (USA).

[7] Swamy RN, Ali SAR. Punching shear behavior of reinforced slab-column connections made with steel fiber concrete. Acids J 1982;79:392–406 (USA).

[8] Narayanan R, Darwish IYS. Punching shear tests of steel-fiber-reinforced micro-concrete slabs. Mag Concr Res 1987;39(N° 138):42–50 (London, UK).

[9] Alexander SDB, Simmonds SH. Punching shear tests of concrete slab-column joints containing fiber reinforcement. Acids Struct J 1992;89(4):425–32 (USA).

[10] Harajli MH, Maalouf D, Khatib H. Effect of fibers on the punching shear strength of slab-column connections. Cem Concr Compos 1995;17:161–70.

[11] Gouveia AV, Lapi M, Orlando M, Faria DMV, Ramos AP. Experimental and theoretical evaluation of punching strength of steel fiber reinforced concrete slabs. Struct Concr 2018;Vol. 19-1:217–29.

[12] Higashiyama H, Ota A, Mizukoshi M. Design equation for punching shear capacity of SFRC slabs. Int J Concr Struct Mater 2011;5(1):35–42.

[13] Maya Duque LF, Fernández Ruiz M, Muttoni A, Foster SJ. Punching shear strength of steel fibre reinforced concrete slabs. Eng Struct 2012;Vol. 40:93–4 (UK).

[14] Aveston J, Kelly A. Theory of multiple fracture of fibrous composites. J Mater Sci 1973;8:352–62.

[15] Hillerborg A. Analysis of fracture by means of the fictitious crack model, particularly for fibre reinforced concrete. Int J Cem Compos 1980;2(4):177–84.

[16] Naaman AE, Nammur GG, Alwan JM, Najm H. Fiber pullout and bond slip. II: experimental validation. ASCE J Struct Eng 1991;117(9):2791–800.

[17] Li VC, Wang Y, Backer S. A micromechanical model of tension softening and bridging toughening of short random fiber reinforced brittle matrix composites. J Mech Phys Solids 1991;39(5):607–25.

[18] Di Prisco M, Plizzari G, Vandewalle L. Fibre reinforced concrete: new design perspectives. Mater Struct 2009;42:1261–81.

[19] Amin A, Foster SJ, Muttoni A. Derivation of the σ-w relationship for SFRC from prism bending tests. Struct Concr 2015:93–105.

[20] Facconi L, Minelli F. Behavior of lightly reinforced fiber reinforced concrete panels under pure shear loading. Eng Struct 2020;202(13).

[21] Cuenca E, Conforti A, Monfardini L, Minelli F. Shear transfer across a crack in ordinary and alkali activated concrete reinforced by different fibre types. Mater Struct 2020;53(15).

[22] Wang XL, Liu YQ, Liu S. Effect of chloride-induced corrosion on bond performance of various steel fibers in cracked SFRC. Cem Concr Compos 2023;140(14).

[23] Moraes Neto BN, Barros JAO, Melo GS. Model to simulate the contribution of fiber reinforcement for the punching resistance of RC slabs. J Mater Civ Eng 2014;26–7 (10).

[24] Venkateshwaran A, Tan KH, Li Y. Residual flexural strengths of steel fiber reinforced concrete with multiple hooked-end fibers. Struct Concr 2018;19–2: 352–65.

[25] Faccin E, Facconi L, Minelli F, Plizzari G. Predicting the residual flexural strength of concrete reinforced with hooked-end steel fibers: new empirical equations. In: Serna P, Llano-Torre A, Martí-Vargas JR, Navarro-Gregori J, editors. Fibre Reinforced Concrete: Improvements and Innovations II, BEFIB 2021. RILEM Book series, Vol. 36; 2021. p. 456–68.

[26] Soroushian P, Lee C-D. Distribution and orientation of fibers in steel fiber reinforced concrete. Acids Struct J 1990;87(5):433–9 (USA).

[27] González DC, Mínguez J, Vicente MA, Cambronero F, Aragón G. Study of the effect of the fibers' orientation on the post-cracking behavior of steel fiber reinforced concrete from wedge-splitting tests and computed tomography scanning. Constr Build Mater 2018;192:110–22.

[28] Barnett SJ, Lataste J-F, Parry T, Millard SG, Soutsos MN. Assessment of fibre orientation in ultra high performance fibre reinforced concrete and its effect on flexural strength. Mater Struct 2010;43:1009–23.

[29] Ozyurt N, Woo LY, Mason TO, Shah SP. Monitoring fiber dispersion in fiber-reinforced cementitious materials: comparison of AC-Impedance spectroscopy and Image Analysis. Acids Struct J 2006;103-5:340–437 (USA).

[30] Stähli P, Custer R, Van Mier JGM. On flow properties, fibre distribution, fibre orientation and flexural behaviour of FRC. Mater Struct 2008;41:189–96.

[31] Suuronen J-P, Kallonen A, Eik M, Puttonen J, Serimaa R, Herrmann H. Analysis of short fibres orientation in steel fibre-reinforced concrete (SFRC) by X-ray tomography. J Mater Sci 2013;48:1358–67.

[32] Pujadas P, Blanco A, Cavalaro S, De La Fuente A, Aguado A. Fibre distribution in macro-plastic fibre reinforced concrete slab-panels. Constr Build Mater 2014;64: 496–503.

[33] Ponikiewski T, Katzer J, Bugdol M, Rudzki M. Steel fibre spacing in self-compacting concrete precast walls by X-ray computed tomography. Mater Struct 2015;48:3863–74.

[34] Zhou B, Uchida Y. Relationship between fiber orientation/distribution and post-cracking behaviour in ultra-high-performance fiber-reinforced concrete. Cem Concr Compos 2017;83:66–75.

[35] Balázs GL, Czoboly O, Lubloy E, Kapitany K, Barsi A. Observation of steel fibres in concrete with Computed Tomography. Constr Build Mater 2017;140:534–41.

[36] Miletic M, Mohana Kumar L, Arns J-Y, Agarwal A, Foster SJ, Arns C, Peric D. Gradient-based fibre detection method on 3D micro-CT tomographic image for defining fibre orientation bias in ultra-high-performance concrete. Cem Concr Compos 2020;129(18).

[37] Medeghini F, Guhathakurta J, Tiberti G, Simon S, Plizzari G, Mark P. Steered fiber orientation: correlating orientation and residual tensile strength parameters of SFRC. Mater Struct 2022;55(18):251.

[38] Mohana Kumar L, Zeng C, Foster SJ. A stereological approach to estimation of fibre distribution in concrete. Constr Build Mater 2022;324(15).

[39] Stroeven P. Morphometry of fibre reinforced cementitious materials. Matér Et Constr 1978;11:31–8.

[40] Dupont D, Vandewalle L. Distribution of steel fibres in rectangular sections. Cem Concr Compos 2005;27:391–8.

[41] Stroeven P. Stereological principles of spatial modeling applied to steel fiber-reinforced concrete in tension. Acids Struct J 2009;106(3):213–22 (USA).

[42] Laranjeira F, Grünewald S, Walraven JC, Blom C, Molins C, Aguado A. Characterization of the orientation profile of steel fiber reinforced concrete. Mater Struct 2011;44:1093–111.

[43] Ferrara L, Ozyurt N, Di Prisco M. High mechanical performance of fibre reinforced cementitious composites: the role of "casting-flow induced" fibre orientation. Mater Struct 2011;44:109–28.

[44] Svec O, Zirgulis G, Bolander JE, Stang H. Influence of formwork surface on the orientation of steel fibres within self-compacting concrete and on the mechanical properties of cast structural elements. Cem Concr Compos 2014;50:60–72.

[45] Conforti A, Cuenca E, Zerbino R, Plizzari G. Influence of fiber orientation on the behavior of fiber reinforced concrete slabs. Struct Concr 2021;22-3:1831–44.

[46] Boulekbache B, Hamrat M, Chemrouk M, Amziane S. Flowability of fibre-reinforced concrete and its effect on the mechanical properties of the material. Constr Build Mater 2010;24:1664–71.

[47] Alberti MG, Enfedaque A, Galvez JC. A review on the assessment and prediction of the orientation and distribution of fibres for concrete. Compos Part B 2018;151:274–90.

[48] Aidarov S, Mena F, De La Fuente A. Structural response of a fibre reinforced concrete pile-supported flat slab: full-scale test. Eng Struct 2021;239(13).

[49] Oslejs J. New frontiers of steel fiber-reinforced concrete. Concr Int 2008;30-5:45–50.

[50] Maturana Orellana A. Estudio teórico-experimental de la aplicabilidad del hormigón reforzado con fibras de acero a losas de forjado multidireccionales (PhD Dissertation). Spanish: Universidad del País Vasco; 2013.

[51] Destrée X, Mandl J. Steel fibre only reinforced concrete in free suspended elevated slabs: Case studies, design assisted by testing route, comparison to the latest SFRC standard documents. Tailor Made Concrete Structures. Amsterdam, Netherlands: International fib Symposium; 2008. p. 437–43.

[52] CEN, EN 14651, 2008. - Test method for metallic fibre concrete - Measuring the flexural tensile strength, European Committee For Standardization CEN, Brussels, Belgium.

[53] Faccin E., 2022. Experimental and analytical study on punching shear strength of steel fibre reinforced concrete flat slabs, University of Brescia, Department of Civil, Environmental, Architectural Engineering and Mathematics, PhD Dissertation, p. 377, Brescia, Italy.

[54] Thermo Fisher Scientific, 2019. Avizo software User's Guide, Konrad-Zuse-Zentrum für Informationstechnik Berlin (ZIB), Version 9, p. 991.

[55] Skarzynski L, Suchorzewski J. Mechanical and fracture properties of concrete reinforced with recycled and industrial steel fibers using Digital Image Correlation technique and X-ray micro computed tomography. Constr Build Mater 2018;183:283–99.

[56] Vicente MA, Mínguez J, González DC. Computed tomography scanning of the internal microstructure, crack mechanisms, and structural behavior of fiber-reinforced concrete under static and cyclic bending tests. Int J Fatigue 2019;121:9–19.